LUND UNIVERSITY

A family of vortex wakes generated by a thrush nightingale in free flight in a wind tunnel over its entire natural range of flight speeds

Spedding, G R; Rosén, Mikael; Hedenström, Anders

Published in:
Journal of Experimental Biology

DOI:
10.1242/jeb.00423

2003

Link to publication

Citation for published version (APA):
Spedding, G. R., Rosén, M., & Hedenström, A. (2003). A family of vortex wakes generated by a thrush nightingale in free flight in a wind tunnel over its entire natural range of flight speeds. *Journal of Experimental Biology*, *206*, 2313-2344. https://doi.org/10.1242/jeb.00423

Total number of authors:
3

General rights
Unless other specific re-use rights are stated the following general rights apply:
Copyright and moral rights for the publications made accessible in the public portal are retained by the authors and/or other copyright owners and it is a condition of accessing publications that users recognise and abide by the legal requirements associated with these rights.
• Users may download and print one copy of any publication from the public portal for the purpose of private study or research.
• You may not further distribute the material or use it for any profit-making activity or commercial gain
• You may freely distribute the URL identifying the publication in the public portal

Read more about Creative commons licenses: https://creativecommons.org/licenses/

Take down policy
If you believe that this document breaches copyright please contact us providing details, and we will remove access to the work immediately and investigate your claim.

LUND UNIVERSITY

PO Box 117
221 00 Lund
+46 46-222 00 00

Download date: 19. Dec. 2025

The Journal of Experimental Biology 206, 2313-2344
© 2003 The Company of Biologists Ltd
doi:10.1242/jeb.00423

A family of vortex wakes generated by a thrush nightingale in free flight in a wind tunnel over its entire natural range of flight speeds

G. R. Spedding[1,*], M. Rosén[2] and A. Hedenström[2]

[1]*Department of Aerospace and Mechanical Engineering, University of Southern California, Los Angeles, CA 90089-1191, USA* and [2]*Department of Animal Ecology, Lund University, Ecology Building, SE-223 62 Lund, Sweden*

*Author for correspondence (e-mail: geoff@usc.edu)

Accepted 2 April 2003

Summary

In view of the complexity of the wing-beat kinematics and geometry, an important class of theoretical models for analysis and prediction of bird flight performance entirely, or almost entirely, ignores the action of the wing itself and considers only the resulting motions in the air behind the bird. These motions can also be complicated, but some success has previously been recorded in detecting and measuring relatively simple wake structures that can sometimes account for required quantities used to estimate aerodynamic power consumption. To date, all bird wakes, measured or presumed, seem to fall into one of two classes: the closed-loop, discrete vortex model at low flight speeds, and the constant-circulation, continuous vortex model at moderate to high speeds. Here, novel and accurate quantitative measurements of velocity fields in vertical planes aligned with the freestream are used to investigate the wake structure of a thrush nightingale over its entire range of natural flight speeds. At most flight speeds, the wake cannot be categorised as one of the two standard types, but has an intermediate structure, with approximations to the closed-loop and constant-circulation models at the extremes. A careful accounting for all vortical structures revealed with the high-resolution technique permits resolution of the previously unexplained wake momentum paradox. All the measured wake structures have sufficient momentum to provide weight support over the wingbeat. A simple model is formulated and explained that mimics the correct, measured balance of forces in the downstroke- and upstroke-generated wake over the entire range of flight speeds. Pending further work on different bird species, this might form the basis for a generalisable flight model.

Key words: thrush nightingale, *Luscinia luscinia*, flight, aerodynamics, wake, wind tunnel, digital particle image velocimetry (DPIV).

Introduction

The problems in understanding bird flight aerodynamics

A complete, correct and/or detailed understanding of the aerodynamic mechanisms of importance in bird flight is complicated immensely by a number of factors. The most basic problem is that flight speeds are sufficiently slow (typical values for the mean forward speed, U, may range from 1–20 m s^{-1}) and the length scales are sufficiently small (mean chord, c, ranging from 1–10 cm), that the effects of viscosity are not ordinarily negligible. This fact can be written more formally by calculating a characteristic value for the dimensionless Reynolds number,

$$Re = Uc/\nu ,$$

where ν is the kinematic viscosity. For U=10 m s^{-1} and c=5 cm, $Re \approx 3\times10^4$. This is an extremely inconvenient number. It lies well below typical values of 10^6 for small planes where viscous effects can safely be presumed to be restricted to thin, attached boundary layers, and it lies well above characteristic values of 10^2 where the flow over the body and in any wake is laminar and well-organised. On the contrary, even at moderate angles of attack, the flow over well-designed aerofoils veers notoriously between separated and non-separated states, with dramatic differences in mean and instantaneous force coefficients as a result. Over and above treatments found in standard aerodynamics texts, one must also account for the fact that in animal flight the wings themselves are moving relative to the body, and furthermore that they are not rotating steadily like a propeller, but are beating up and down, accelerating and decelerating with each cycle. To this one adds the effects of flexible wing surfaces that not only have complex geometric descriptions, but also significantly change their shape during the wing beat cycle. Although it is straightforward to compile long lists of complicating factors, it is not clear which of them are important, and why and when.

Mechanical or numerical models that slavishly mimic each property lack generality while elegantly simplified analysis might simply be irrelevant.

Describing fluid motions by the vorticity field

An attractive alternative to measuring or predicting aerodynamic forces on odd-shaped bodies with high-amplitude, unsteady motions is to investigate instead the air motions in the wake that are caused by the body (the term 'body' here is used in the general sense to mean solid body, and it includes all wings and appendages). It is frequently convenient to describe fluid motion by its vorticity ω,

$$\omega = \nabla \times \mathbf{u} , \quad (1)$$

where **u** is the velocity vector. Both ω and **u** are vector fields, and ω is a measure of the direction and magnitude of the local rotation in a fluid; it is exactly twice the local angular velocity. Textbooks such as Batchelor (1967, p. 92) and Lighthill (1986, p. 43) speak clearly and elegantly about the analysis and description of fluid motions in terms of the vorticity. Here, we note that a non-zero component of vorticity accompanies any shearing motion in a fluid, and so a description of **u** in terms of ω is not only convenient mathematically, but is also directly connected to the mechanical strain deformations associated with work being done on the fluid particles.

A further mathematical convenience is to speak of vortex lines, which are three-dimensional curves along which |ω| is constant. In a homogeneous fluid without viscosity, there are restrictions on how vortex lines can be arranged and, if and when the vortex lines are collected in simple groups or clusters, then a description of the fluid motion in terms of its vortex lines can be quite economical. The strength of a vortex is measured by its circulation,

$$\Gamma = \int \omega . d\mathbf{S} , \quad (2)$$

which is the vorticity integrated over a material surface, **S**. When the vortex geometry is simple, then identification of a suitable surface is simple also, and in aerodynamics applications, Γ can be related quite readily to integrated or localised forces on the wing.

Applying these methods to the aerodynamic analysis of bird flight holds out the promise of replacing a very large and intricate computation, involving highly unsteady motion of very complex geometries, with a much simpler description of the distribution of wake vorticity. The unsteady forces on the wings themselves are either inferred or ignored as mechanical and energetic quantities are calculated directly from the wake footprint which, by Newton's laws, must contain the integrated history of the forces exerted by the body on the fluid. In particular, the kinematics of the wings themselves are important only in so far as they produce a certain disturbance in the wake.

The basis for theoretical models of bird wakes

Are bird wakes actually composed of simple collections of vortex lines? The first and most well-known of the mechanical models of bird flight is the actuator disc model, expounded by Pennycuick (1968a, 1975) and others. Here the bird is entirely replaced by an idealised circular disc, which acts to accelerate air across it, and deflect it downwards. Implicitly the wake is indeed composed of collections of vortex lines, as the uniformly accelerated flow is separated from the unaffected ambient by a tube of circular cross-section, composed of all of the vortex lines in the otherwise undisturbed flow. The simplicity is extreme, but has made it the most widely used and robust of calculation methods in use today (e.g. Pennycuick, 1989). Some context and consequences of the actuator disc modelling strategy are considered in Spedding (2003). Note that since the kinematics of the beating wings have been disposed of entirely, the model can have little to say about the consequences of variation in wingbeat amplitude, frequency or cyclic variations in planform geometry – all topics of potential interest. Moreover, the infinite tube is unlikely to be a very close approximation of the actual wake.

The first serious attempt to construct an aerodynamic model of bird flight based on a realistic wake structure was by Rayner (1979a–c), who proposed that each wingbeat was only aerodynamically active on the downstroke. The starting and stopping vortices produced at the beginning and end of this downstroke were connected by a pair of trailing vortices shed from the wingtips, and so the wake was composed of a series of vortex rings, or more accurately, elliptical loops. This sounds deceptively simple, and the process cartooned in Fig. 1 gives some indication of the assumptions required and likely complexities.

The vortex ring model was entirely theoretical, having no experimental support, although it clearly represented an improved picture from the old vortex tube, and was argued from reasonable grounds. It received independent support in experimental work published that year by Kokshaysky (1979), who showed that cross-sections through clouds of sawdust in the wakes of small passerines revealed ring-like structures, with one shed per wingbeat. The technique was not a quantitative one, however, and so certain critical quantities such as wake momentum and energy could not be verified. The vortex ring model received further support in quantitative reconstruction of three-dimensional tracks traced by clouds of neutrally buoyant, helium-filled soap bubbles for pigeons in slow (U=2.4 m s^{-1}) flight (Spedding et al., 1984), and for a jackdaw in similar conditions (U=2.5 m s^{-1}; Spedding, 1986). In both cases, however, the measured wake momentum was insufficient to provide weight support, and it was tentatively concluded that some as yet unidentified complexities in the wake structure or its measurement were responsible for this seeming paradox, which has remained unresolved.

Unexpectedly, experiments with the same apparatus on kestrel flight at moderate (U=7 m s^{-1}) speeds (Spedding, 1987b) showed no wake momentum deficit and no vortex rings either. Instead of discrete loops separated by aerodynamically inactive upstrokes, two continuous undulating vortex tubes were found, one trailing behind each wingtip, and without strong concentrations of starting or stopping vortices cross-

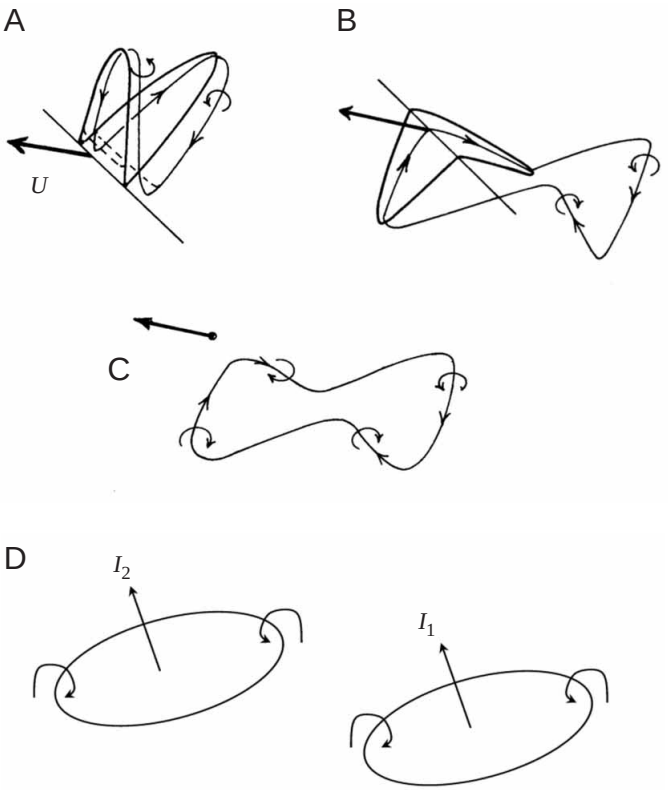

Fig. 1. The generation of a single, closed-vortex loop during a downstroke can, in principle, lead to a simple wake model geometry. The bird body (which has no aerodynamic significance) is represented by a stick supporting the wings. The assembly moves at constant speed, *U*. As the wings accelerate at the beginning of the downstroke (A), they shed vorticity into the near wake, which rolls up as a concentrated starting vortex. During the downstroke (B), the starting vortex remains connected to the two wingtip vortices, which elongate as the downstroke progresses. At the end of the downstroke, the wings decelerate, shedding vorticity into the wake along the trailing edge, and then vanish (C), taking no further part in the aerodynamics until they reappear at the beginning of the next wingbeat. The hypothetical deformed loop left at C then relaxes into, or can be modelled by, a planar ellipse, and the idealised model wake (D) is composed of a sequence of these, separated by spaces left by the inactive upstroke. Although this wake-generation mechanism is ostensibly simple, the details are not, and numerous assumptions about the formation, shedding and subsequent roll-up of vortex lines or tubes with complex curvature are built in. *I*, wake impulse; circular arrows indicate the local sense of rotation of the induced flow.

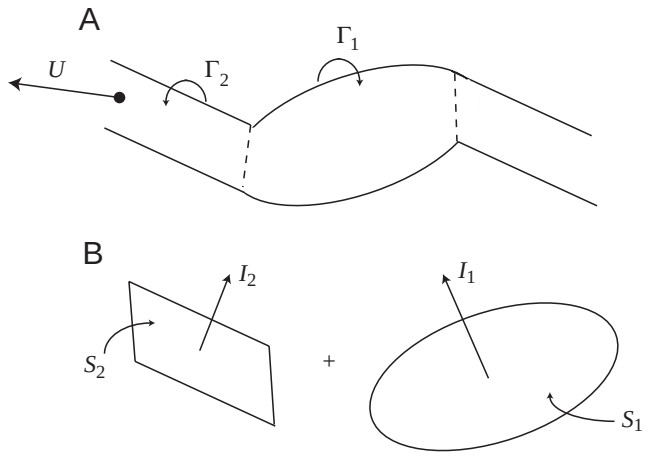

Fig. 2. Constant-circulation wake. In (A), the effect of the (invisible) bird moving at speed *U* is to leave behind a pair of undulating vortices with constant circulation (Γ_1=Γ_2=constant), in which case potential cross-stream vortices denoted by broken lines have zero strength. Here the geometry is simplified for convenience so the wake appears as if the downstroke and upstroke portions were approximate ellipses and rectangles, respectively, as drawn in (B). Although the actual geometry assumed in most models (e.g. Rayner, 1986; Spedding, 1987b) is slightly more complicated, the fundamental principle remains that the wake impulse (*I*) from both down- and upstrokes points upward, contributing to lift, and hence weight support. Because the wingspan is reduced on the upstroke, the projection of area S_1 onto a vertical plane will be larger than that of S_2, and so the net impulse of the whole wake is forward, generating thrust.

linking the two. The measured circulation of the shed vortices was the same on down- and up-strokes, supporting this interpretation, and a net thrust was achieved by the variation in wake width due to flexion of the primary feathers during the upstroke. A cartoon of a constant-circulation wake model is shown in Fig. 2. This was a qualitatively new kind of wake structure, and while vortex rings might seem like a favourable configuration because they convey the maximum momentum per unit kinetic energy, the constant-circulation wake would also appear to be advantageous in minimizing the shedding of cross-stream vorticity. (The cross-stream vorticity is not absent, but occurs in the curvature of the downstroke trailing vortices.) In order to generate net thrust some variation in impulse must occur, but it is through varying the wing geometry, and not through varying the circulation on the remainder of the wing that continues to take part in the aerodynamics. These results were originally described in a thesis (Spedding, 1981), and the same experimental apparatus was subsequently used to visualise wakes of noctule bats, but without quantitative measurements (Rayner et al., 1986). At slow speeds (1.5, 3 m s^{-1}), the bubble tracks were interpreted to be tracing discrete rings or loops, while at higher speeds (7.5 m s^{-1}) the patterns seemed closer to the constant-circulation geometry seen in the kestrel.

Other than isolated photographs in review-type articles or books (e.g. in Norberg, 1990; Rayner, 1991a,b; Spedding, 1992), this remains the sum total of experimental evidence on the structure of vertebrate wakes in flapping flight. There are some obvious gaps to fill; for example, on how it is that wake patterns transition from one form to another. Spedding (1981, 1987b) cautioned against interpolating between only two data points, but speculated that intermediate wake forms between constant-circulation and closed-loop wakes might involve the gradual increase in strength of cross-stream vortices, as shown in Fig. 2. Rayner (1986, 1991a,b, 2001), on the other hand, has proposed that all bird wakes must be either one of the two

forms (closed-loop or constant-circulation) and that these constitute two separate gaits, analogous in some respects to terrestrial gaits, of horses, for example.

Current status

To date, there have been no quantitative data on bird wakes at more than one particular flight speed for the same individual or species. Furthermore, all existing quantitative studies are based on the three-dimensional bubble-cloud seeding technique, where large parts of the overall wake volume can be simultaneously observed, but at the expense of rather low spatial resolution. Typically, 2500 bubble traces were recorded over a volume of approximately 600 mm×600 mm×400 mm (numbers from Spedding et al., 1984; Spedding, 1986), which is equivalent to a mean inter-bubble spacing of 27 mm in each direction, comparable to mean core radii of 35 mm and 30 mm for the vortex rings observed in the pigeon and jackdaw experiments, respectively. The inconsistent quantities at slow flight speeds could have been caused by structural details whose presence would only be discernible at higher resolution, and the assumptions forced upon the experimental analysis by the limited spatial resolution might closely reflect assumptions in the model under test, thereby rendering the test non-independent. Recalling the first part of this introduction, one might be especially wary when Reynolds numbers are in the range where quite disorganised and turbulent motions might be anticipated at small scales (of the order of a core radius), and in some cases at large scales (of the order of a mean chord, *c*) too.

Objectives

This paper reports on the results of an extensive series of experiments in measuring bird wakes over a continuous range of flight speeds in a low-turbulence wind tunnel. The measurement technique has been customised extensively for this particular application and offers improvement in spatial resolution by a factor of 10 and a similar improvement in accuracy of estimation of velocity fields and their spatial gradients. A companion paper (M. Rosén, G. R. Spedding and A. Hedenström, in preparation) describes the detailed wing kinematics of the same bird flying under the same conditions, allowing connections between the wingbeat and wake structure to be deduced. Here the motion of the wings themselves is ignored almost entirely, and we focus on a correct reconstruction of the most likely three-dimensional wake structure. Qualitative and quantitative changes in wake structure with flight speed will be presented. At most flight speeds, the wake is dissimilar to those previously reported and the consequences will be discussed.

Materials and methods

The experiment

The experiment and its data analysis methods are quite new, and their design, implementation, validation and performance analysis are given in some detail in Spedding et al. (2003). A brief summary only will be given here.

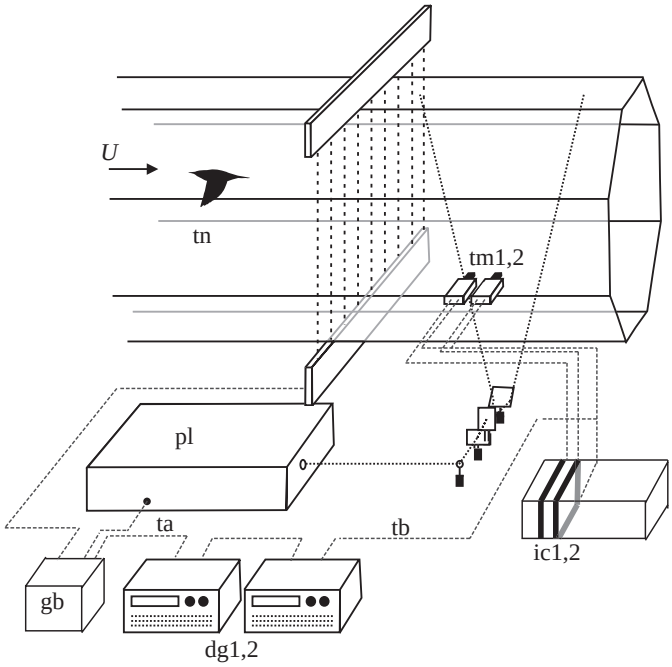

Fig. 3. The bird (tn) is trained to fly at constant speed, *U*, the independently controlled speed of the wind tunnel. Two Stanford DG 535 delay generators (dg1,2), configured to run off a single crystal base timing clock, generate synchronised timing pulses to control the dual-head Nd:YAG (pl) laser output flash timing (ta) and the asynchronous reset (tb) for the two CCD array cameras (tm1,2). The timing of the reset pulses is determined by the mean speed, *U*, and by the downstream displacement of tm2 from tm1, and is designed to remove the mean flow from the measured displacement field. Digital images are acquired at independent interface cards (ic1,2) and transferred directly to PC RAM. The laser timing pulses are gated (gb) with the summed output from an array of LED-photodiode pairs so that if any one or more beams are interrupted by the bird, laser output stops. (Modified from Spedding et al., 2003.)

Apparatus and bird training

Experiments were carried out using a closed-loop, low-turbulence wind tunnel designed for bird flight experiments (Pennycuick et al., 1997), and the general setup is shown in Fig. 3. Four juvenile thrush nightingales *Luscinia luscinia* L. were caught in southern Sweden on migration in August 2001, and brought to the wind tunnel aviary in Lund. After a period of acclimatization, daily flight training began, and soon revealed that two, and eventually one, bird would fly for prolonged periods in the test section. The bird was trained to sit on a perch that could be lowered for take-off and flight, and raised before landing. The bird was trained to fly at a position near the centre of the test section in low light conditions with an upstream luminescent marker as the sole reference point. The training was prolonged and rigorous, beginning more than 2 months prior to experiments, and progressing in conditions that gradually resembled the experiment, beginning with low ambient light conditions, and eventually to the introduction and maintenance of fog particles and occasional bursts of high intensity laser light.

Table 1. *Morphological data for* Luscinia luscinia

		Units	Mean value	Uncertainty
Semispan	b	cm	13.1	0.5
Wing area	S	cm^2	126	5
Mean chord	c	cm	4.8	0.2
Aspect ratio	AR		5.4	0.3
Body mass	m	g	30.5	0.5
Wing loading	Q	$N\ m^{-2}$	24	0.6

The laser was a Quanta Ray PIV II, dual head Nd:YAG from Spectra Physics, with a maximum flash intensity of 200 mJ $pulse^{-1}$, although it was used mostly at about 120 mJ. The timing between pulses in a pulse-pair can be as little as 1 ns. Settings of 100–500 μs were used in all experiments reported here. The double-pulsed laser beam was spread into a planar sheet by a sequence of converging and then two cylindrical lenses, before reflecting off a 45° inclined front surface mirror into the test section through a clear Plexiglass panel (Fig. 3).

A vertical grid of infrared LED-photodiode pairs was arranged so that if any beam was interrupted by the bird, the laser pulses would be automatically suspended. The flight speed, U, varied between 4 and 11 $m\ s^{-1}$, air density was 1.17–1.25 $kg\ m^{-3}$ and the temperature 16–20°C. From previous wind tunnel calibration data, turbulence intensities were calculated to be <0.06% of U in the speed range used (Pennycuick et al., 1997). These levels are too low to be measured directly by digital particle image velocimetry (DPIV) methods themselves (see Spedding et al., 2003).

Tables 1 and 2 give some basic morphological data together with some common aerodynamic performance measures for this experiment.

Wind tunnel corrections

The bird is small compared with the wind tunnel test section, and interactions with the side walls can be ignored. This can be demonstrated with a simple lumped vortex model of a thin airfoil (Katz and Plotkin, 2001, p. 119), from which one can write an expression for the modified lift, L', due to presence of solid boundaries in a confined duct of height h:

$$L' = L\left(1 + \frac{\pi^2}{24}\frac{c^2}{h^2}\right). \quad (3)$$

The magnitude of the correction is negligible ($<10^{-2}$) for all values of $c/h \leq 0.2$, which is true even when the span, $2b$, is taken as a length scale. This criterion perhaps should be taken as a lower limit, because possible proximity of the wake to the tunnel walls at the measuring station is of equal importance. In fact, it will be seen that the wake growth rates in both the y (spanwise) and z (vertical) directions were interestingly low, and corrections based on subsequently measured wake widths at the measuring station did not exceed 2×10^{-2} (2%).

Analysis

Properties of Correlation Imaging Velocimetry (CIV)

The two laser pulses were imaged onto two Pulnix TM9701N full-frame transfer CCD array cameras, in upstream-downstream sequence. The digital image pairs (768×484×8 bits) were analysed using a custom variant of standard DPIV methods, known as Correlation Imaging Velocimetry (CIV). The collection of CIV techniques is described in detail in Fincham and Spedding (1997). CIV was developed to maximise the accuracy of estimation of very small particle displacements, regardless of computational cost. Arbitrary sized and shaped cross-correlation boxes can be defined and are completely decoupled from the similarly arbitrarily defined search domain. No FFTs (Fast Fourier Transforms) are used in the computation, and sub-pixel displacements can be estimated to $1/50^{th}$ pixel in the best case. In practice, one can expect $1/20^{th}$ pixel uncertainty. When mean pixel displacements are 5 pixels, the uncertainty is approximately 1%, and the velocity bandwidth is 1:100. In order to profit from the advanced numerical techniques it is essential to properly control/select the value of the timing interval, δt, between exposures of the two images in a pair. In this two-camera variant, δt is partly determined by the mean flow and camera separation so that the mean displacement field is zero. δt is then tuned, on top of this value, to ensure that disturbance quantities (i.e. displacements due to the bird wake) fill out the range of displacements up to 5 pixels. Constraints on this calculation are the three-dimensional, cross-plane motion in the wake, and the light sheet (or slab) thickness, which is set to between 3–4 mm.

Customisations for bird flight measurements

Because the two successive images come from two separate cameras, there are extra distortions introduced by having two different lenses and two slightly different (unavoidably, within the manufacturing tolerances of the cameras) camera geometries, effective focal lengths and optical axis orientations. An extensive series of tests (described in Spedding et al., 2003) with test backgrounds of pseudo-particles and pseudo-displacement fields, allowed the CIV calculations themselves to be used to compute a mean distortion field at the same, or higher, resolution as the experimental data. The test or residual fields can be stepwise ramped up in complexity, from stationary object to fixed displacement, to moving object, to wind tunnel background

Table 2. *Dimensionless numbers at low and high flight speeds*

		Flight speed U ($m\ s^{-1}$)	
		4	11
Reynolds number	$Re=Uc/\nu$ ($\times10^4$)	1.3	3.5
Reduced frequency	$k=\pi fc/U$	0.53	0.19

c, mean chord; ν, kinematic viscosity; f, wingbeat frequency.

flow. Finally, in the last stage, the flying bird is added to the set-up, and only differences between this case and the background flow are computed. Thus, the effects of optical misalignments and distortion are automatically compensated for, and the CIV calculation bandwidth is focused entirely on the wake displacement field due to the presence of the bird and its beating wings.

The disturbance displacement fields are calculated with 20–24 pixel correlation boxes, overlapping by 50% to yield pixel displacements on a nominally rectangular 58×54 grid, with aspect ratio one, and resolution of approximately δ=3.5 mm. Note that δ is comparable to the light sheet thickness, which governs the averaging distance normal to the plane. The sampling volume is thus roughly cubical. This field is corrected for the finite displacement of the source correlation box and the flow is reinterpolated onto a grid with the same dimensions, using a two-dimensional, thin-shell smoothing spline. Adjustment of the smoothing parameter allows certain nonphysical displacement errors (if present) to be removed. The smoothing parameter is equivalent in the spline formulation of specifying a non-zero viscosity for the fluid (for details, see Spedding and Rignot, 1993), and does not involve any neighbourhood-averaging, which would be guaranteed to underestimate peak gradient quantities. Spatial gradients are calculated directly from the spline coefficients without recourse to further smoothing or averaging.

The analysis is performed in a frame of reference moving with the mean speed, U, and u, v and w are velocity components in the streamwise (x), spanwise (y) and vertical (z) directions in this reference frame. (This choice of coordinate system reflects the most common one for aerofoil or aircraft analysis, where y is almost always a spanwise location.) Data were taken in vertical planes aligned with the freestream. The bird would sometimes take up slightly different positions in y, or would drift slowly. With the position of the light slice fixed, its location relative to the bird could be checked from standard video images taken by a camera downstream of the test section. Silhouettes of the bird were visible against the bright vertical stripes of the over-exposed laser sheet image. The slice positions were categorised as centre/body, left/right midwing, left/right wingtip and left/right outer field, as illustrated in Fig. 4. All data described in this paper come from vertical slices at centre/body, left midwing and left wingtip. (Data from left and right wings did not differ, and there were many fewer right wing data runs as they represent unusually large departures from the standard position for the bird.)

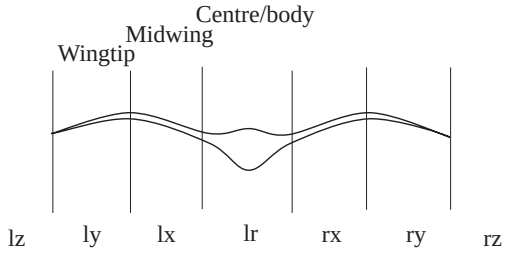

Fig. 4. Classification of all spanwise locations by character code (bottom) and the three named categories appearing in this paper, centre/body (lr) , midwing (lx) and wingtip (ly).

Safety considerations required the leftmost point of the data (governed by the left margin of the right camera image, which was determined by the light sheet fan-out and x-location) to be approximately 84 cm downstream of the bird. The wake left behind during the course of a wingbeat extends downstream by a distance $x_c=Ut_c$, where t_c is the evolution time of this wake segment. So, if that time is a wingbeat period, T, then a wake wavelength, λ is

$$\lambda = UT . \tag{4}$$

The wingbeat frequency changes rather little as U ranges from 4–11 m s^{-1} (M. Rosén, G. R. Spedding and A. Hedenström, in preparation), so λ increases steadily with increasing U. The downstream measuring location is 2–3λ at U=4 m s^{-1}, and only 1λ at U=11 m s^{-1}.

Quantitative analysis and wake-specific measurements

In each vertical slice, we have velocity components u and w as functions of x and z. These can be argued to be the most interesting components: since w is parallel to the gravitational vector, $\boldsymbol{g}$, it describes the momentum changes and forces that counteract $\boldsymbol{g}$. Similarly, variations in u are directly related to the fore–aft forces on the bird, which are the drag and thrust, opposed to, and aligned with the direction of motion. From the data the only measurable component of vorticity (Equation 1) is the spanwise vorticity ω_y, normal to the plane of the light slice,

$$\omega_y = \frac{\partial w}{\partial x} - \frac{\partial u}{\partial z} . \tag{5}$$

The y subscript will occasionally be dropped for clarity. Since it is primarily maps of $\omega_y(x,z)$ that will be used to describe the wakes, it is very important to estimate this quantity as accurately as possible and to know the likely uncertainty. A usual rule of thumb for reasonable (and credible) estimates of uncertainty in gradient quantities in fluid flows of moderate complexity is ±10%. For rather more rigorous and quantitative statements of the likely uncertainties in application of the CIV method, see Fincham and Spedding (1997). Here, the extra care taken in isolating the disturbance field (which contains all the vorticity), and in saturating the measurement bandwidth through appropriate choice of δt, gives a likely uncertainty in ω_y of ≤5%. This is discussed in detail, with evidence from extensive control experiments, in Spedding et al. (2003).

The predicted maps of $\omega_y(x,z)$ for ideal vortex loop and constant-circulation models (Figs 1 and 2) are shown in Fig. 5. Vertical cuts through a vortex loop should show two vortex cross-sections of equal strength for all vertical cuts except those at the wingtip, where disturbances on top of the streamwise vortices might be visible. By contrast, centreplane cuts through the constant-circulation wake should show almost nothing at all. Moving away from the centreline, cuts through

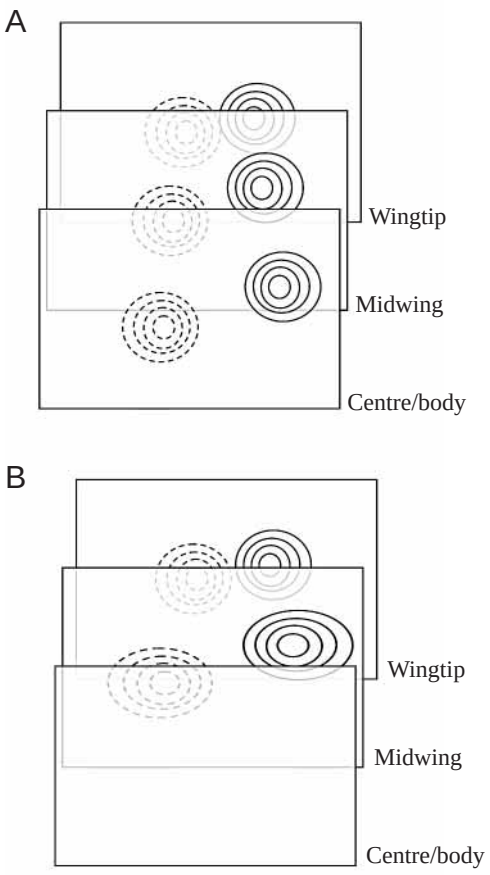

Fig. 5. Idealised predicted spanwise vorticity $\omega_y(x,z)$ in vertical cross-sections through (A) the vortex loop and (B) the constant-circulation wake models of Figs 1D and 2, respectively. Although sections further towards the wingtip cut more obliquely through the presumed vortex lines, the effect on peak $|\omega_y|$ measurements would be small, and in A the sections through the closed loop are shown with unchanged amplitude. (The *circulation will* be unchanged.) If the wake has continuous trailing vortices (as in the constant-circulation model), then at the centreplane $|\omega_y|=0$ (B). Midwing cuts may have more complicated cross-sectional geometries if, as anticipated, they cut through transition regions between down and upstroke-generated vortices.

the upper and lower curved branch of the trailing downstroke vortex should be seen. The wingtip pattern will look much the same as for the closed-loop.

When and if the data do not conform to simple predicted geometries, the main challenge is in performing the inverse of Fig. 6, deducing the most likely three-dimensional structure based on stacks of two-dimensional slices. It is not impossible to do this, partly because of a classical result in mathematics due to Helmholtz, showing that in a homogenous field/fluid, objects such as vortex lines must either terminate at a boundary or form closed loops on themselves. When combined with the symmetry of the wing and body geometry and of the normal wingbeat kinematics, this quite strongly constrains (i) the number of possible vortex wake topologies that could plausibly be produced, and (ii) the number of self-consistent interpretations of limited data, such as vertical centreplane slices, or stacks of slices from centreline to wingtip. If, for example, in Fig. 5A the peak value, or integrated magnitude, of the cross-section contours of spanwise vorticity changes from slice to slice, then some component of streamwise vorticity must exist to account for the difference. If, on the other hand, the diagnostic values do not change within measurement uncertainty, then the most parsimonious explanation is that the cross-sections are passing through a single structure that intersects both measurement planes. It is the application of this reasoning that allows iterative testing and re-evaluation of postulated three-dimensional structures in the wake, so not only can existing theories be tested, as illustrated in Fig. 5, but new wake geometries can also, in principle, be proposed.

It is comparatively simple to measure the strength of the vortex cross-sections by making a discrete approximation of Equation 2 as

$$\Gamma_A = \sum_i \sum_j \omega_y(i,j)dxdy\,, \tag{6}$$

where the strength (circulation) of vortex A is calculated from the sum of all contiguous cells where ω_y exceeds some threshold value, such as 20% of its maximum. The calculation is robust and simple, but difficulties can arise when the area occupied is very diffuse, and the result must additionally be constrained to be inside some local spatial area. Moreover, using a fixed-fraction threshold ensures that some low-amplitude contributions will be omitted, and so controlling the unruly spread of vortex A by imposing a high threshold increases the severity of this underestimate. Here, we assume that the true distribution of below-threshold vorticity is something like a similarly thresholded Gaussian function, *G*. For this, or any other known or presumed functional form, one can calculate the fraction omitted for any arbitrary fixed threshold, and add that to the sum of Equation 6. For example, for the normalised Gaussian function with amplitude, *A*, and half-width, σ,

$$G(r) = \left(\frac{A}{\sqrt{\pi 2\sigma^2}}\right) e^{-\frac{r^2}{2\sigma^2}}, \tag{7}$$

where *r* is the radial distance from the centre, then the fraction of *G* above threshold T_G (where T_G varies from 0 to 1) is

$$G^+_{T_G} = G(1 - T_G)\,. \tag{8}$$

When T_G=0.2, the above-threshold fraction of *G* is 0.8 of its total. This is the procedure followed for all estimates of circulation Γ reported herein. Threshold values of 20% of the local maximum ensure that directly summed values remain above any likely noise level and the correction represents a reasonable compromise in presuming and/or estimating the contribution of the low-amplitude tails of the distribution.

For economy of presentation, normalised measures of $|\omega_y|_{max}c/U$ for positive and negative-signed vortices will be named Ω^+ and Ω^-, and their corresponding normalised

circulations, Γ/Uc, will be denoted Γ^+ and Γ^-. Means for a particular flight speed and span location will be denoted by overbars in the text if the context is otherwise ambiguous. All error bars in the figures show standard deviations (S.D.).

Results

Reconstruction of the vortex wakes

The vortex wake structure will be reconstructed from series of vertical slices for three flight speeds, U=4, 7 and 10 m s^{-1}. As will later become clear, there is no special significance to these speeds, and they are used as examples of low, medium and high speed flight over the range 4–11 m s^{-1} achievable by the thrush nightingale. Measurements are summarised as combined velocity and vorticity fields, with velocity vectors shown amplified (the arrow length corresponds to some factor greater than one times the real spatial displacement over the exposure time δt) and halved in spatial resolution. These are superimposed upon $\omega_y(x,z)$ mapped onto a discrete colourbar‡ whose effect is to show colour contours, where the contour interval is commensurate with the claimed measurement uncertainty in ω_y. Thus, if a feature can be seen in the data, it probably does exist.

More than 4000 velocity fields have been analysed over the range of flight speeds, and there is no way to show all of the supporting evidence and measurements for all of the reconstructions. The slow-speed case will be presented in some detail, and then subsequent cases will be summaries only, even though they have been based on similar amounts of both qualitative and quantitative evidence.

Deducing the wake structure from multiple vertical slices at different spanwise stations is an iterative process. Plausible, but temporary conceptual models of the wake structure are formulated and tested through repeated inspection and measurement of large numbers of velocity/vorticity maps. Qualitative models guide quantitative tests, which in turn support or contradict the models. The presentation of the qualitative wakes data precedes the quantitative measurements in this paper, because appreciation of the former is required to understand the significance of the latter. For this reason, the qualitative reconstructions will be summarised and completed in this section, requiring a certain amount of interpretation to be mixed in with the raw data. The benefit is that the conceptual and physical models can act as an organising structure within which the significance of the extensive quantitative measurements can be understood and evaluated.

‡The strong colour contrasts that are independent of signal intensity on the discrete colourbar make it difficult to interpret at first. However, it has been deliberately chosen to accomplish four specific objectives: (1) To render the plots quantitative. Any point on any of the plots can be selected and the value of the vorticity can be looked up on the colour table. If specific shades of colour are difficult to discern, the neighbouring colours can be used to unambiguously identify values. This transforms the plots from qualitative descriptions to quantitative ones, particularly in view of the next point. (2) The colour-step resolution matches the numerical resolution of the vorticity calculation itself. Thus, the uncertainty in assigning a colour, and hence numerical value, to a point is equal to the uncertainty in calculating that quantity. (3) The colour table works primarily by means of contrast in hue, but it is accompanied by luminance contrast, and so works also in black and white (grey-scale). (4) Since the discrete steps impose a linear scale on the perceived field (as opposed to rainbow-type continuous bars which rely on the nonlinear mapping of the human visual system), then low intensity features can be distinguished as well as high intensity ones. Later, it will become clear that the distribution of low amplitude vorticity is of critical importance in this study. Further points in colour mapping of fluid mechanical quantities are considered by Farge (1987, 1990).

Slow speed (U=4 m s^{-1})

Fig. 6 shows four consecutive frames of the vertical centreplane velocity and vorticity fields. Since the wingbeat frequency is approximately 14 Hz (at all flight speeds) while the sampling rate, determined by the maximum laser repetition rate, is 10 Hz, each frame shows a portion of the wake from a different wingbeat, slightly phase-shifted, so the wake self-samples as it is advected by the mean flow past the fixed cameras. The starting vortex at the left of Fig. 6A is succeeded in Fig. 6B by another which is shifted to the right (increasing x). In the next frame (Fig. 6C), no starting vortex is visible, the whole frame being occupied by upstroke-generated motions. Subsequently (Fig. 6D) a third starting vortex appears. Approximately 4.2 wake periods have passed by the cameras in four frames. The wingbeat frequency f calculated from this phase-shifted time series is 14 Hz. f calculated from high-speed video kinematic analysis is 14.2 Hz.

A second interesting consequence of these phase-shifted data is that, to some extent, the degree of steadiness of the wingbeat can be inferred from the repeatability of the wake pattern. Thus we note that while the starting vortex is always the most visible object in the wake, its location in z does not change very much. The wake structure is quite level, and the flight must have been also. This can now be turned into an important criterion for further selection of data, since the only other control on the bird position is months of training. If, and only if, a wake pattern is repeated along the 10 Hz sampling sequence, then the data are accepted as having come from steady level flight.

Regarding the vorticity field itself, it is immediately obvious that positive-signed, starting vortices (or those so-presumed) are significantly higher in amplitude and more coherent than their negative-signed counterparts. This is always the case, without exception, and the sequence shown here is completely typical in this regard. The two frames showing upstroke-generated vorticity (Fig. 6A,C) show very broadly distributed, low amplitude (but measurable) traces with little clear structure.

The asymmetry in peak vorticity is readily quantifiable, as in Fig. 7, where a simple time series is plotted of the strongest absolute value vorticity in each frame. Values shown as filled circles come from the remnants of starting vortices and those as open circles from the stopping vortices appearing at the end of the downstroke. Not only are the peak values different, by a factor of 3–4, but the total integrated circulations (also plotted as squares in Fig. 7) are different too, albeit by a smaller amount. It is not simply that the same amount of vorticity has been spread over a larger area; the total amounts are apparently different. We will later revisit this topic in some detail.

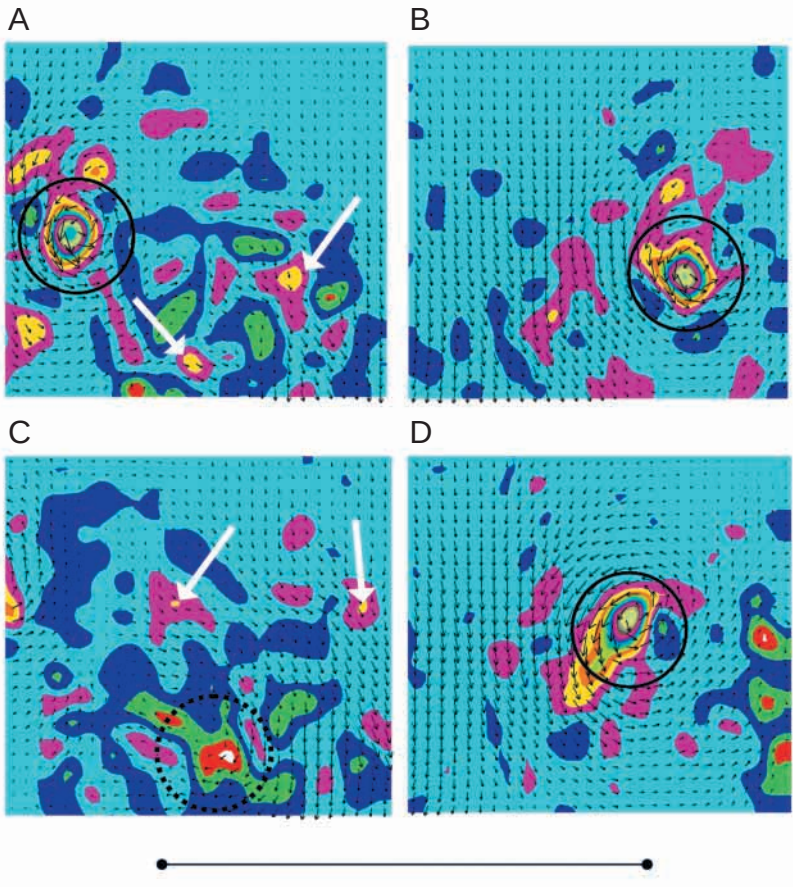

Fig. 6. (A–D) Four consecutive fields of $\omega_y(x,z)$ with velocity vectors superimposed at half their true spatial resolution. The reference frame is moving with the mean flow, and so it is as if the bird had passed from right to left, leaving behind these traces in still air. The colour bar intervals correspond roughly to the measurement uncertainty. The colour bar is scaled asymmetrically about ω_y=0, and the numbers at the ends show values in units of s^{-1}. The circle-ended line shows the scale of the wingspan, 2*b*. The window size $\Delta x,\Delta z$ is approximately 20 cm×18 cm. The circles drawn around locally maximum positive values of $\omega_y(x,z)$ show the regions within which normalised circulation Γ^+ is calculated. Γ_{tot} is calculated by including all above-threshold values in the same frame, regardless of whether they are within the local neighbourhood, or connected. Similarly, the negative peak is identified by the broken circle. The trailing vorticity attributable to the upstroke contains both negative and positive local peaks (large white arrows). In A these low-amplitude, positive peaks will be included in the sum for Γ_{tot} (because they have the same sign as the peak value), but in C, they will not. The development of an accounting procedure that correctly accounts for the real (as opposed to idealised) measured vorticity distributions is given in Figs 27 and 28 and their associated text.

A more compact and easily interpretable summary of the data of Fig. 6 is given in Fig. 8, where segments of the time series have been patched together to show the spatial structure of the wake from one complete wingbeat. Since each frame is a phase-shifted view of a repeated wake structure, neighbouring frames are overlaid with the first in time located rightmost, and passing right to left through the original time series. Although the detailed structure varies somewhat from wingbeat to wingbeat, this basic wake pattern is seen in all centreplane slices. None of the vortices are perfectly circular in cross-section, the starting vortex is significantly more compact and pronounced than the stopping vortex, and although there are trails of negative vorticity continuing on into the upstroke (again, this is always the case), qualitatively, it appears quite weak. By implication, the upstroke is mostly aerodynamically inactive. Other than the weak stopping vortex, a closed-loop wake model with most or all aerodynamically useful forces occurring on the downstroke would be a reasonable approximation of this structure.

Close inspection of the overlay of velocity vectors and the vorticity map shows that the two are misaligned. Fig. 9 shows an enlargement of the rightmost starting vortex cross-section, now with the true number of vectors reinstated. The centre of rotation does not coincide with the peak in vorticity. Fig. 10 shows the profiles of $u(z)$ and $w(x)$ drawn through the peak in ω_y. Although ω_y is defined by these gradients of $\partial u/\partial z$ and $\partial w/\partial x$, the zero crossings do not occur at the vortex centre. The effect is particularly evident in $\partial w/\partial x$, where the asymmetry of

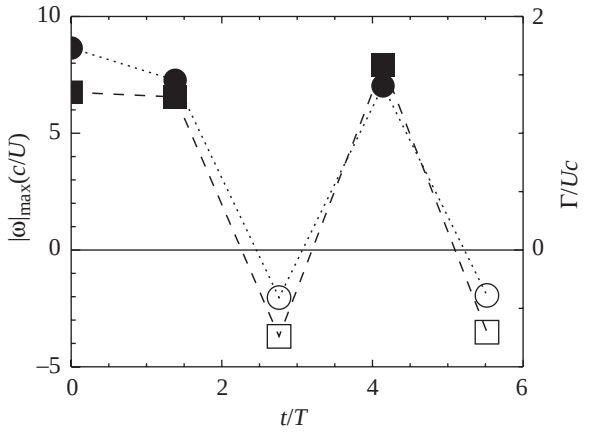

Fig. 7. The peak absolute value of the spanwise vorticity $|\omega|_{max}$ (circles), rescaled by the wing chord *c* and mean speed *U* as a function of time *t* in wingbeat periods *T*. The normalised circulation Γ (squares) is also plotted on the second ordinate. Filled symbols, positive vortices; open symbols, negative ones. The first four time steps correspond to the data in Fig. 6. The time series represents successive sections of the wake passing through the observation window. The field is strongly asymmetric in both the peak vorticity and its integrated total strength.

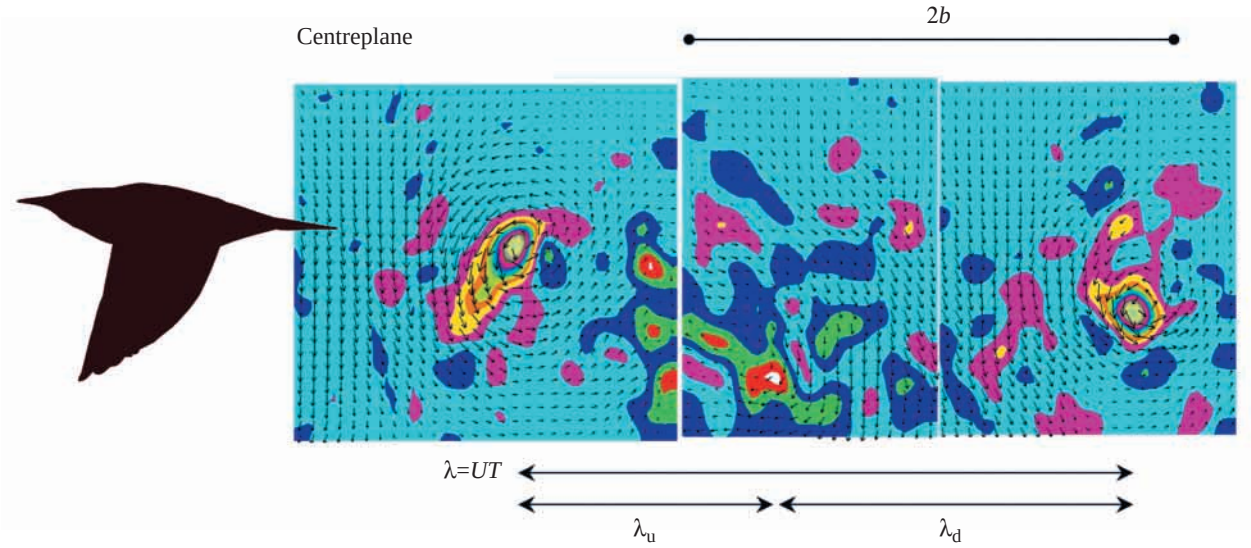

Fig. 8. A reconstruction from three consecutive frames of Fig. 6 to show the vortex wake over slightly more than one wingbeat cycle. The wake is shown as if left in still air by the bird passing from right to left. The silhouette is drawn approximately to scale and in the correct vertical (z) position but its horizontal (x) location should in fact be displaced by about 3λ to the left (upstream) because the measuring station is that far downstream of the bird in the test section. During the time required for the wake to advect past the cameras (approx. 3T, or 0.21 s), the wake has moved downwards under its self-induced convection speed. The three component frames are matched approximately but the data are not edited or reinterpolated to improve the fit, and the borders are left outlined so their location is clear. The wingspan bar (2b) is placed to begin at the start of the downstroke. The wake wavelength is determined by the flight speed and wingbeat period and is shown as a double-arrowed bar. The relative time spent on downstroke and upstroke is given by the downstroke ratio, and can be verified from the wake picture. The colour bar and its scaling are as given in Fig. 6, and are fixed for all low-speed wake images (Figs 6, 8, 9, 11).

the profile about its centre is also clear. Towards the left, downward velocities are higher and the peak gradient is shifted in that direction. A misalignment will occur whenever the observation reference frame does not move with the mean self-convection speed of the vortex structure itself (imagine adding a uniform mean flow to any structure – the vorticity is unchanged but the location of flow reversal in the vector field changes). The misalignment will also occur when a measurement slice is taken obliquely through a straight-line vortex with circular core cross-section, or through one with a curved arc, because in the interior (x–x_0<0), the induced flow is influenced by a closer source than on the exterior. If the geometry were known in advance, then the relative shift in the peak ω_y and the centre of rotation could be used to calculate the curvature or incidence angle, respectively. Here, the mean convection speed is small (compared with the peak induced flow speed) and uniform across the span, and the mismatch between peak vorticity and flow reversal and its spanwise variation supports the conceptual model of a curved vortex loop.

Fig. 9. Magnified view of the rightmost starting vortex in Fig. 8. The apparent centre of rotation deduced from the arrows does not lie on the peak of the spanwise vorticity.

Figs 9 and 10 demonstrate that the spatial resolution is sufficient to estimate these subtle effects and to measure the shear gradients with low uncertainty (as previously claimed in Materials and methods). A shift by one grid point left–right (±x) or up–down (±z), as shown by the dotted lines very close to the solid line profiles in Fig. 10, makes very little difference to the profile gradients. There are approximately seven points across the core in each profile, and the core diameter defined by the distance between velocity peaks is approximately 2 cm in both x and z.

An equivalent reconstruction to Fig. 8, but for the midwing and wingtip sections, is given in Fig. 11. At the midwing (Fig. 11A), the two vortex cross-sections are now separated by a smaller distance, consistent with intersections further out through a curved structure. The stopping vortex has a higher

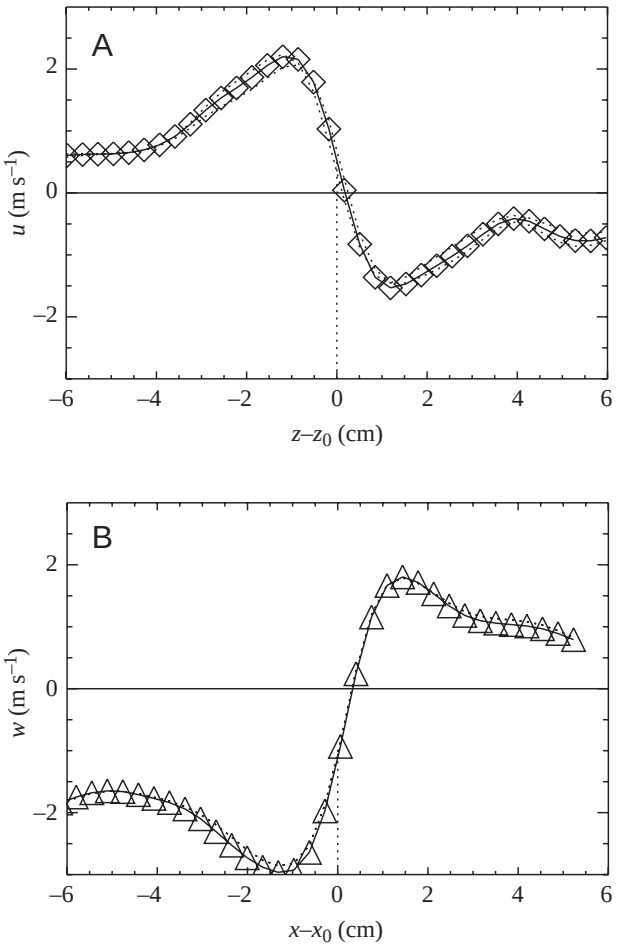

Fig. 10. Profiles of the velocity components $u(z)$ (A) and $w(x)$ (B), where (x_0,z_0) is the location of the peak in ω_y. The vertical dotted lines projected from $z=z_0$ and $x=x_0$ intersect the curves of $u(z)$ and $w(x)$ slightly offset from the $u=0$ and $w=0$ lines. Original data points are shown as diamonds (A) and triangles (B), joined by straight lines. Just noticeable are dotted line curves that join profiles either side of x_0 and z_0, respectively.

peak value, both relative to the starting vortex, and absolutely, as shown by the black saturation of the lower end of colour bar. As in Fig. 8, there is little coherence in the upstroke regions, and no systematic shrinking of their streamwise extent in cross-section as we proceed from wing root to wingtip. The starting vortex cross-section at midwing, however, is more complex than closer to the centreline, appearing double-, or even triple-peaked. Again, this is quite characteristic of the many (250) midwing wake sections analysed at this flight speed. The outer region of the vortex loop is altogether less coherent (in this cross-section) than at the centreline.

The three-dimensional picture is completed by the wingtip reconstruction of Fig. 11B. From the starting vortex (left), which has a quite distinct second peak, the more complex cross-sectional structure noted in the previous figure is maintained. The stopping vortex is again more distinct than in the more central sections, but also has two strong peaks. There are some trace negative patches in a cloud around the main stopping vortex, but nothing at all in the upstroke part.

The evidence accumulated from the vertical sections at three spanwise locations points to a relatively simple vortex topology, where the majority of the vorticity (and circulation) is contained within a curved loop traceable to the downstroke. If this is the primary structure then the circulation of the vortices should be the same in each section. Fig. 12 shows the peak vorticity and the circulation of the strongest vortex in the data comprising the reconstructions of Figs 8 and 11. The peak vorticity Ω^+ and circulation Γ^+ of the positive (starting) vortices does not change significantly from wing root to wingtip. Neither does Ω^-. However, the magnitude of Γ^- increases towards the wingtip. This confirms: (i) that the starting vortex loop is continuous and unbranched, and (ii) that during the downstroke the shed vorticity becomes more diffuse, not all of it collected in a single concentrated lump. This numerically confirms what was already qualitatively readily apparent in Fig. 8, but with consistent support from the off-centre slices.

Fig. 13 summarises the most likely three-dimensional topology of vortex lines making up the slow-speed wake. It is a simplification, but has the following essential properties: (i) the initial starting vortex is concentrated, (ii) during the downstroke, vortex elements become separated, (iii) the stopping vortex is quite diffuse, with elements trailing into the upstroke, and (iv) the upstroke nevertheless does not appear to generate significant coherent motion.

Medium speed ($U=7$ m s^{-1})

Characteristic patterns of $\omega_y(x,z)$ for the centreplane, midwing and wingtip sections are shown in Fig. 14A–C. Fig. 14A is a composite of several frames. It shows a surprising, but quite characteristic, new wake structure that can be seen at a number of flight speeds. The upstroke is aerodynamically active, as judged by the downwash inclined normal to a complex upstroke-generated vortex structure that is distinct from the downstroke vorticity. The cross-section through the upstroke wake is complex, but has mostly positive vorticity at the beginning and mostly negative vorticity at the end. This suggests that a different circulation (it must drop towards the end of the downstroke and then increase again at the beginning of the upstroke) is established on the wings during the upstroke, so that the whole wake is a sequence of alternating structures from up- and downstrokes.

At midwing (Fig. 14B), the only trace of the upstroke structure is from the small upward induced flow. Vortex cross-sections can have complicated geometry, and there is an interesting mix of positive and negative patches at the junction between down- and upstroke. A similar composite, more towards the wingtip (Fig. 14C), shows another complex mosaic of positive and negative patches at this junction. Upward-induced flows can be detected at the beginning and end of the upstroke region where the section is closer to the main wake structure. The most likely collection of vortex lines to account

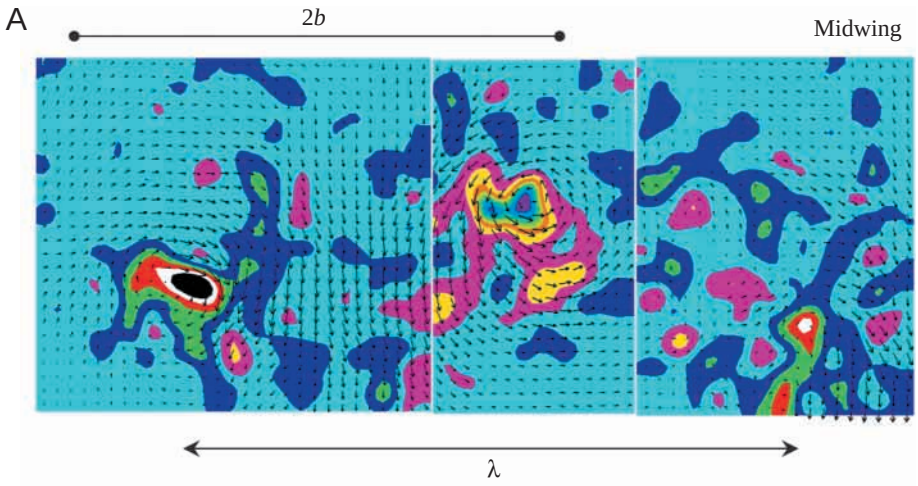

Fig. 11. (A) Vertical cross-section through a midwing plane in the 4 m s^{-1} wake. Plotting conventions are as described in Figs 6 and 8, so relative bird motion is from right to left. The colour bar scaling is fixed to that established in the centre plane (Fig. 6), so saturation of the negative part indicates a relatively stronger stopping vortex contribution. (B) Vertical cross-section through the wingtip plane in the 4 m s^{-1} wake. A and B, together with Fig. 8, can be compared with the three idealised patterns of Fig. 5.

for these figures (and many others like them) is shown in Fig. 15. Each repeating wake segment (one per wingbeat) contains two conjoined closed-loop structures. The way in which the slow-speed wake evolves into this one is by the increase in relative strength of the cross-stream vortices associated with the upstroke. It does so gradually as the speed increases. Note that while the relative magnitude increases, the absolute value does not, as the colour bar scaling for the negative vorticity component has decreased from –250 s^{-1} to –160 s^{-1} (cf. Figs 6 and 14).

High speed (U=10 m s^{-1})

At high speeds (Fig. 16), the mapping of $\omega_y(x,z)$ at the centreplane (Fig. 16A,B) onto the locally rescaled colour bar shows measurable cross-stream vorticity at almost every instant during both upstroke and downstroke. No single structure or pair dominates, and there is a quite seamless transition between the down- and upstroke-generated downwash. The wake wavelength, $\lambda=UT$, continues to increase (inevitably). Fig. 16B also shows a second section through the downstroke–upstroke transition that is closer to the true centreline than the main composite, and the absence of any large/strong stopping vortex is notable. Progressing further out towards the midwing (Fig. 16C,D), the strongest downwash (flow moving mostly vertically downwards) is confined to the downstroke. Already the upstroke trailing vortex is inboard of this section and very little disturbance can be seen during this wingbeat phase. The vorticity distribution can be quite complex as shown in Fig. 16D. The large black region in the section through the negative vortex shows that the fixed colourbar scaling established by the centreline section has been saturated. It is much easier to identify both starting and stopping vortices than was the case at the centre/body section. The oblique cut through the stopping vortex in both (Fig. 16C,D) then runs through the upwards-induced flow induced by the vortex that has projected through the page

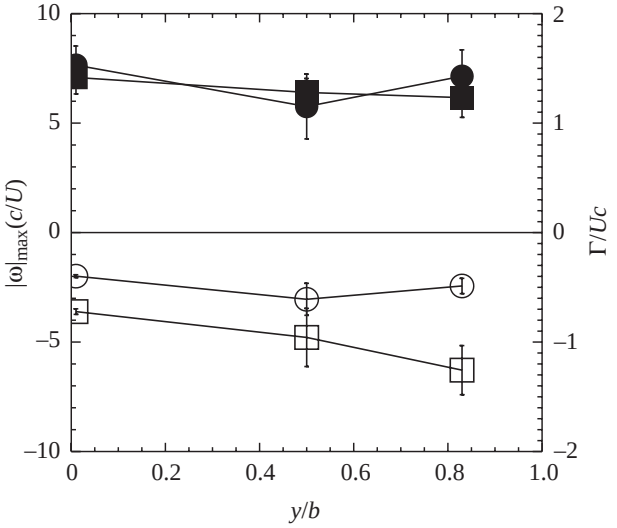

Fig. 12. Variation in peak vorticity magnitude $|\omega|_{max}$ (circles) and circulation Γ (squares) rescaled by the wing chord c and mean speed U for positive (filled symbols) and negative (open symbols) vortices in the slow-speed wake as a function of spanwise distance divided by the semispan y/b.

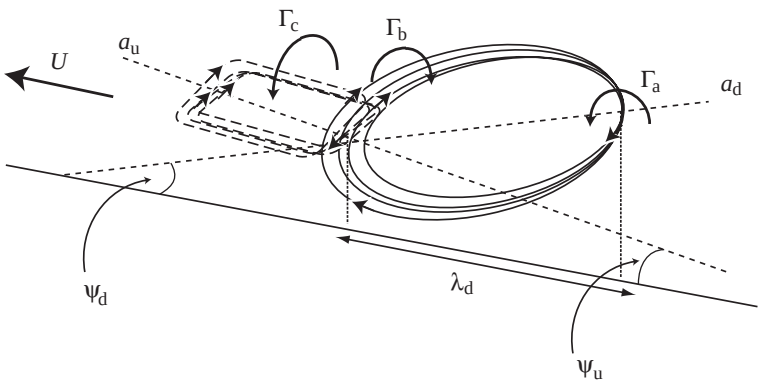

Fig. 13. A possible representation of the slow-speed wake by a small number of vortex lines, based on data such as Figs 8, 10–12. The primary wake structure is a collection of loops, drawn as solid ellipses. They intersect the centre/body plane of observation along the major axis marked a_d, which makes an angle ψ_d with the horizontal (downstroke; a_u, ψ_u, respectively, for upstroke). Γ_a is the measured strength of the starting vortex. Γ_b is the total measured strength of the more diffuse collection of vortex lines left at the end of the downstroke. Γ_c is small compared with both Γ_a and Γ_b, and the collection of rectangular upstroke wake vortices (broken lines) is an idealised cartoon version of the observed trace patterns that are quite disorganised and weak. Their primary effect is to disrupt the structure of the measured stopping vortex, which they do because vortex lines of opposite sense lie close together. When their strengths go to zero, a standard closed-loop wake model results. The projection of the downstroke wake length in x, λ_d, onto the centreline is denoted by the double-headed arrow. U is the mean flight speed; bold arrow indicates direction of flight.

towards the viewer. Further out towards the wingtip (Fig. 16E,F), there is only a downward and then upward induced flow at the downstroke-generated portion.

The sections of Fig. 16 are consistent with steadily moving outwards through a curved vortex structure that does not all meet at the centreline, but mostly extends on into the upstroke. The pattern in Fig. 16E also shows a shear layer developing above the obliquely cut wingtip vortex, with two locations where vectors point from right to left. This component is probably a viscous drag wake that is entrained along the vortex core. In high-speed wakes it is very common to see this close to the wingtip, and the free shear layer instabilities riding on top of the core structure are also common. It is doubtful whether the instabilities themselves have any impact on the bird, but the viscous drag wake is an important component of the force balance at high speeds.

Fig. 17 shows the most likely wake structure based on Fig. 16, completing the three samples of the family of wake structures. The tentative three-dimensional wake models of Figs 13, 15 and 17 are based on these and other data, and also on certain of the quantitative results in the following section, where quantitative data are organised primarily towards making estimates of wake impulse and momentum balance at different flight speeds. Some of these results, however, particularly involving circulation estimates at different spanwise locations, provide strong support for the reconstructions in this section (as also noted in Fig. 5 and its discussion), which were only completed following this analysis.

The wake reconstructions are based on assemblages of independent vertical slice data from multiple wingbeats, and this procedure only works if the flights themselves are steady and repeatable. Mostly, the predominant structures self-select because they can be seen repeatedly on hundreds of occasions, but there are exceptions whose appearance can be traced to some unusual (in this context) flight behaviour. Before proceeding with the quantitative analysis of the proposed wake structures in steady flight, two non-standard examples will be briefly given, first because they shed some light on the normal wake structures and their interpretation, and second because they point to further studies of important flight modes.

Other wakes

Fig. 18 shows the vertical centreplane wake for a brief period of gliding flight at 11 m s^{-1}. The patches of largest $|\omega_y|$ mark a wake that extends straight back behind the bird. Here and elsewhere, the velocity field is dominated by the induced downwash, which in general points downward and backward. Fig. 19A shows a vertical profile of the streamwise-averaged horizontal velocity,

$$U_X(z) = \frac{1}{n_x} \sum_{i=1}^{n_x} u(x_i,z) , \qquad (9)$$

where the sum at each vertical z location is taken over all the discrete streamwise data points, x_i, in the field of view. The leftwards pointing peak represents the departure from the mean profile due to the body drag.

Fig. 19B shows the streamwise distribution of vertically averaged, vertical velocities,

$$W_Z(x) = \frac{1}{n_z} \sum_{j=1}^{n_z} w(x,z_j) , \qquad (10)$$

where the sums are accumulated as for Equation 9. The mean flow is downwards ($\bar{W}_z$=–70±20 cm s^{-1}), becoming less strong with increasing downstream distance, x. The smaller scale oscillations superimposed on the mean decay come from the vertical profiles passing through different structures in the wake that deflect the velocity vectors (leftwards on average, Fig. 19A) from their mean downward orientation. The mean downwash magnitude can, in principal, be used to check on the mean vertical impulse of the gliding wake.

Fig. 20 is a single wake image from a vertical plane, just off the centre flight line, for flight at 9 m s^{-1}, when the bird was briefly gliding and adjusting its position in the test section. As in Fig. 18, the largest $|\omega_y|$ values lie on a nearly horizontal line with mean flow from right to left, representing a net drag. The

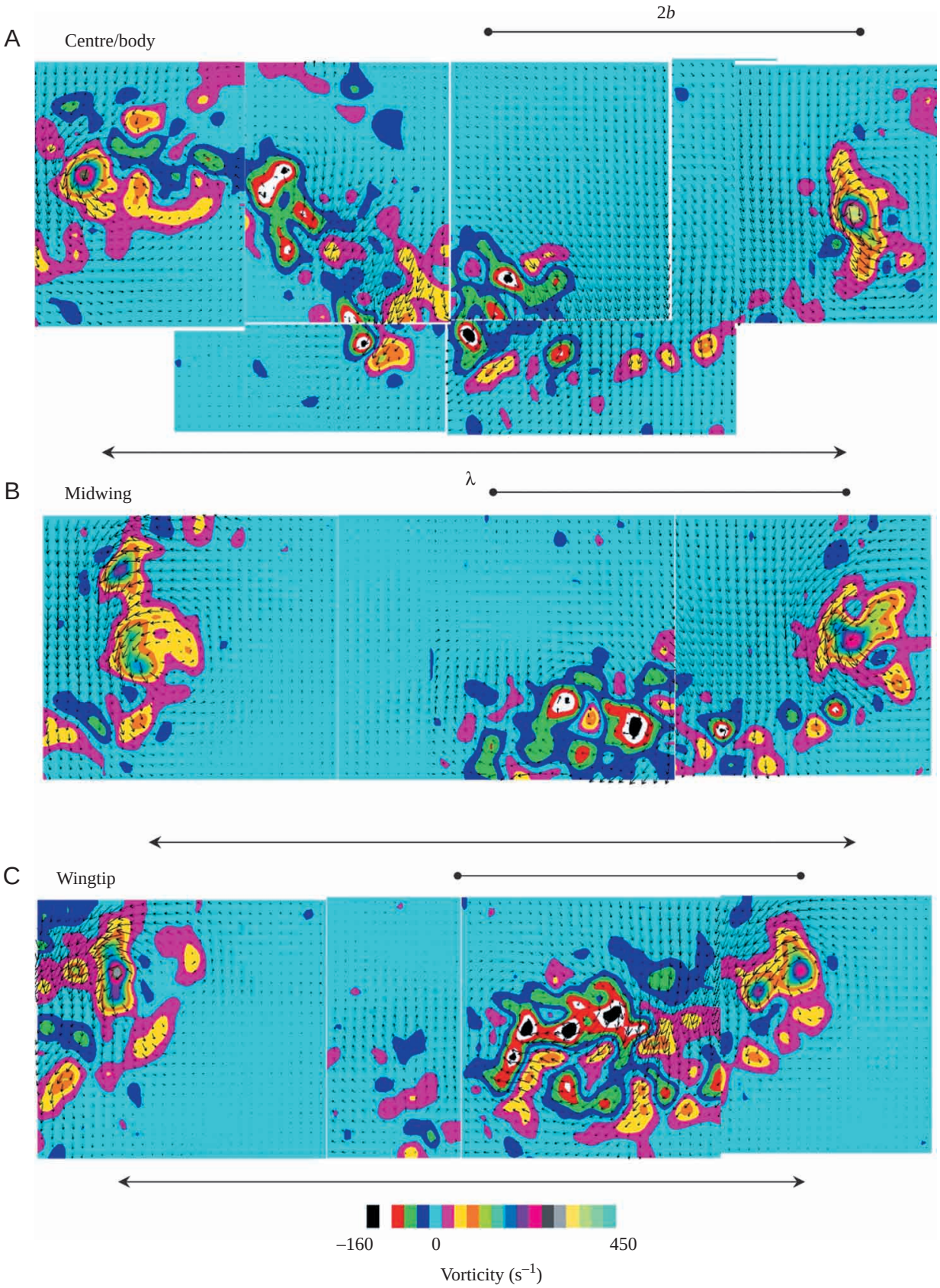

Fig. 14. Composites of the wake at moderate speed U=7 m s^{-1}. The plotting conventions are as previously given in Fig. 8. The colour bar scaling is fixed for all centreplane (A), midwing (B) and wingtip (C) sections.

downwash is much stronger in the upper half-plane, quite different from the steady wakes data and from the gliding example of Fig. 18. The wake defect (Fig. 21) is also much larger than the straight gliding case (Fig. 19A). The high-drag wake of Fig. 20 comes either from the body and tail, or from trailing-edge shedding, close to the wing root, of a partially stalled wing during manoeuvre. The two cases cannot be distinguished unambiguously here, but the roughly equal amplitudes and number of structures with positive and negative sign argue for the former.

Figs 18 and 20 isolate the contributions of body and tail to the wake structure since the wings are beating with small amplitude and acceleration, if at all. These wakes are qualitatively different from the flapping wing wakes in the standard reconstructions. The body wake disturbance itself (Fig. 18) is of very low amplitude (Fig. 19) and cannot usually be detected amongst the much stronger disturbances generated by the wings. It need not be considered further in the following momentum balance calculations.

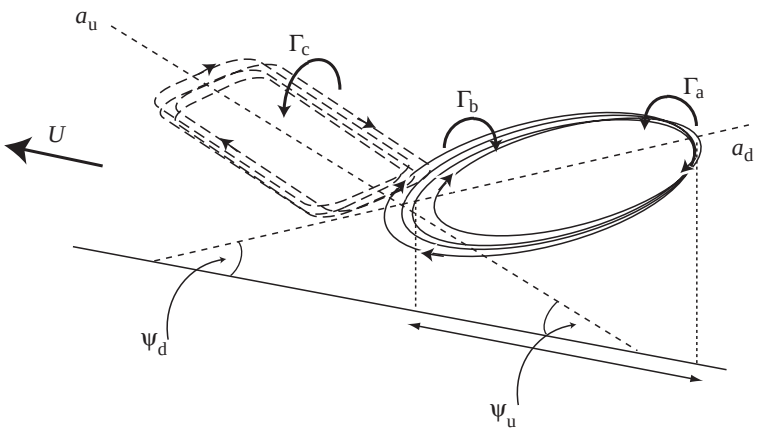

Fig. 15. Most likely wake topology deduced from all data at U=7 m s^{-1}. The basic form is quite similar to the low-speed wake in Fig. 13 (the symbols and notation are the same), but the upstroke-generated portion (broken lines) is stronger, and more distinct from the downstroke-generated loops (solid ellipses).

Wake impulse and momentum balance

Calculation of wake circulation, impulse and reference quantities

Having established a qualitative picture of the wake structure, the peak spanwise vorticity $|\omega_y|_{max}$ and the circulation, Γ, of a structure in cross-section were measured for all fields appearing to be part of a steady level flight segment. There were 1261 of these.

In the following plots, the measured circulations are normalised in two ways. Most obviously, one might divide by a reference Γ_0, which is the circulation that would be required for a wing of equal span in steady flight to support the weight. This can be readily calculated since the Kutta–Joukowski theorem gives a simple relation between the lift per unit span L' and the circulation,

$$L' = \rho U \Gamma \,, \tag{11}$$

where ρ is air density. As a rough approximation, ignoring the effects of induced drag and of variable circulation on the wing, then the weight W must be balanced by the total lift as,

$$W = L = \rho U \Gamma_0 2b \,. \tag{12}$$

This is equivalent to the assumption that a rectangular flat wake provides the vertical impulse, without the reduction in effective span by tip vortices, and without the inclination angle required to overcome induced drag. The correction factor for an elliptically loaded wing is $\pi/4$. It is preferable to avoid adding untestable assumptions about the circulation distribution, and so the uncorrected reference circulation is

$$\Gamma_0 = W / \rho U 2b \,. \tag{13}$$

Conceptually, it is the idealised value required for weight support in steady, gliding flight, provided by the rectangular wake shed directly from the wingtips.

Alternatively, one might consider the case where all of the weight support derives from the impulse of elliptical vortex loops, one shed per downstroke (Fig. 1D). The vertical impulse, I_z, is given by the product of the projection onto the horizontal plane of the planar area of the vortex loop with its circulation,

$$I_z = \rho S_e \Gamma_1 \,, \tag{14}$$

and the projected loop area is

$$S_e = \pi b(\lambda_d/2) \,. \tag{15}$$

λ_d is the horizontal wavelength of the downstroke,

$$\lambda_d = UT\tau \,, \tag{16}$$

for a stroke period T and downstroke ratio, τ. In steady flight, the weight is balanced by the average impulse per unit time, and so the reference value, Γ_1 can be written

$$\Gamma_1 = WT / \rho S_e \,. \tag{17}$$

Both Γ_0 and Γ_1 are simple to calculate and give references against steady gliding flight (without regard to generation of thrust) and against downstroke-only derived closed loops. These quantities are useful conceptually, even though neither model is particularly well-supported by the data presented in the previous section.

Γ_0 and Γ_1 both decrease with flight speed, U, as the problem of providing sufficient impulse can be spread over an area that increases with U. In fact, there is a simple relationship between Γ_0 and Γ_1 determined by the geometry of the flat wake and the projected ellipse. To see this, one may rewrite Equation 13 slightly:

$$\Gamma_0 = WT / \rho UT 2b \,, \tag{18}$$

so the denominator is the product of the air density $\rho \times$ the rectangular wake area generated every stroke period, $UT2b$.

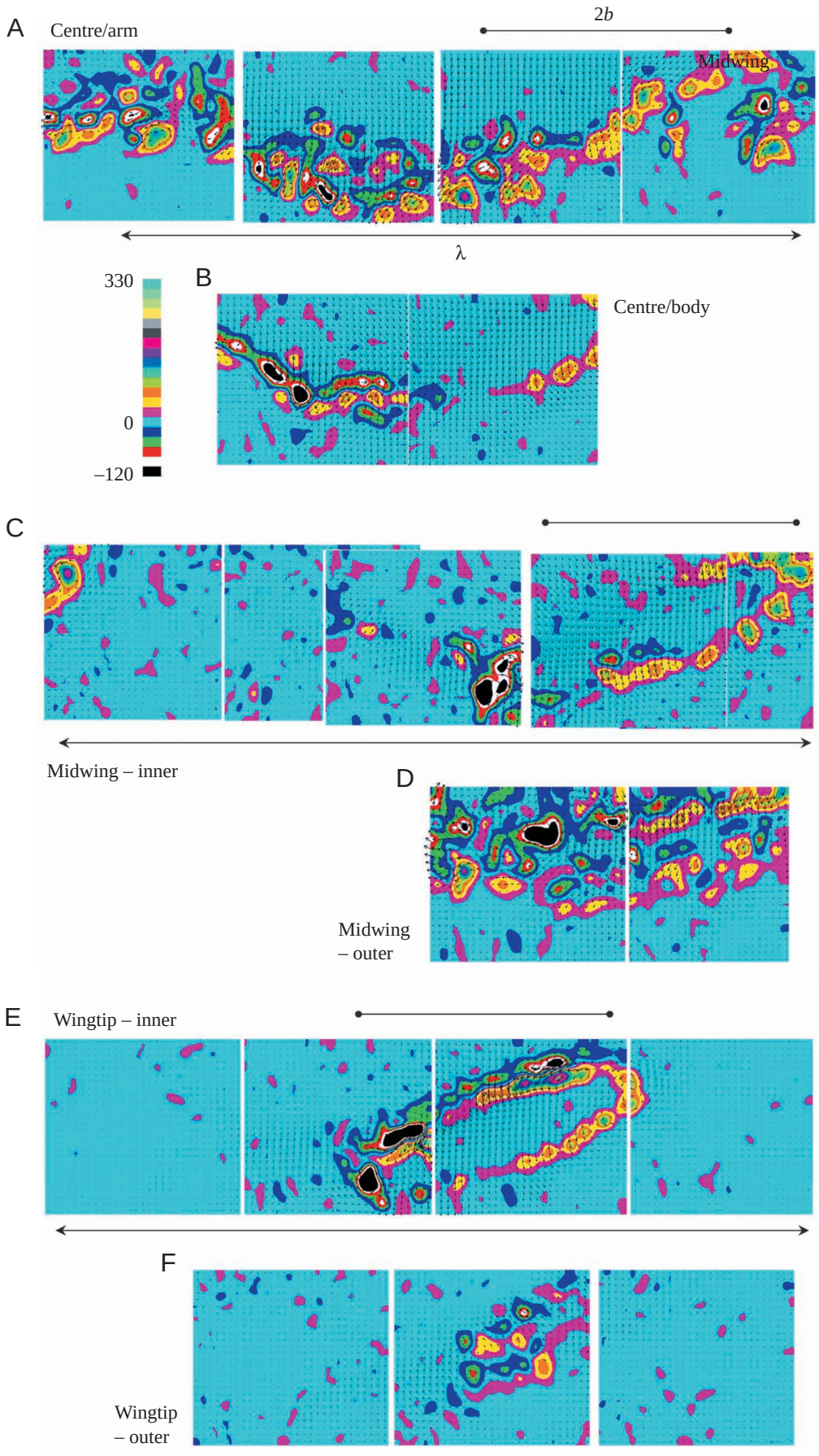

Fig. 16. (A) Composite for high-speed (U=10 m s^{-1}) flight, close to the vertical centreplane, but slightly offset, showing the structure over an entire wavelength. (B) Closer to the true centerline. (C,D) Similar sections through proximal and distal midwing locations; (E,F) the same for the wingtip section.

Combining with Equation 17, the ratio of the two circulations is:

$$\Gamma_0 / \Gamma_1 = S_e / UT2b , \quad (19)$$

which is just the ratio of the projected wake areas. Simplifying, this ratio depends on τ alone,

$$\Gamma_0 / \Gamma_1 = (\Pi/4)\tau , \quad (20)$$

and for τ=0.6, $\Gamma_0/\Gamma_1 \cong \frac{1}{2}$. Γ_0 needs to be only about one half of Γ_1 because the projected area of the wake is larger by approximately a factor of two.

Individual measurements of vortex patches in low-, medium- and high-speed wakes

Fig. 22 shows the distribution of measured circulation *versus* peak spanwise vorticity for all measurable vortex cross-sections in steady flight at U=4 m s^{-1}. A measurable cross-section is defined as a contiguous above-threshold region surrounding a local peak value in $\omega_y(x,z)$. Characteristically there will be one of these in any single frame, either of positive or negative sign, from structures created at the beginning and end of the downstroke, respectively. Each sum in Equation 6 is made around the peak value in the whole frame, and the thresholding and correction procedure described in Equations 7 and 8 is then applied. Example areas and

peak values are shown superimposed on the raw data in Fig. 6.

In Fig. 22, the closed symbols show positive-signed elements (from the starting vortex) and the open symbols are for the negative-signed ones (stopping vortex). At the centre/body sections (Fig. 22A), the range of Ω^+ (peak vorticity of positive sign) is larger than the equivalent range of Γ^+ (the circulation associated with the peak maximum positive vorticity), whose values lie close to Γ_0, but (or, given Equation 20, consequently) not close to Γ_1, the reference most pertinent to this wake geometry. The open symbols for the stopping vortex are significantly lower in magnitude, in both Ω^- and Γ^-. They are quite closely clustered around the mean in Ω^-, as compared with the Ω^+ values. Throughout Fig. 22, the Ω^- distributions are more compact than their Ω^+ counterparts, which is opposite to the degree of compactness, or coherence, of the spatial distributions of $\omega_y(x,z)$. Proceeding through midwing (Fig. 22B) to wingtip (Fig. 22C), the distribution of starting and stopping vortices begins to overlap slightly, as the centroids of each cloud (horizontal and vertical solid

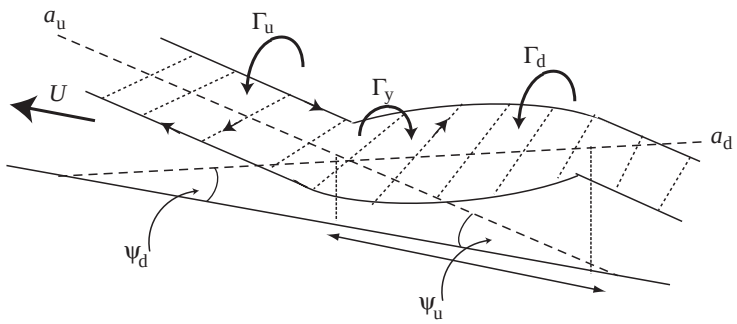

Fig. 17. Most likely collection of vortex lines for the high-speed wake, based on data such as shown in Fig. 16. Now the primary wake structures are primarily oriented in the streamwise direction and there is no preferred location for the comparatively weak cross-stream vortices Γ_y. The correctness of this structure can be determined by testing whether Γ_d=Γ_u. For an explanation of other symbols, see Fig. 13.

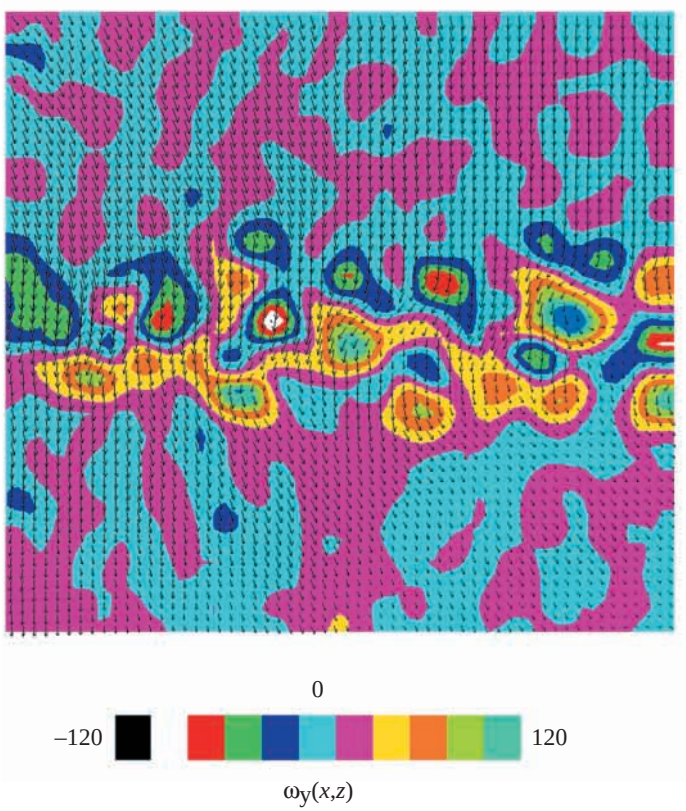

Fig. 18. Single-frame view of the wake during brief gliding interval at 11 m s^{-1} flight speed. The velocity field is dominated by the induced downwash. The cross-stream vorticity, $\omega_y(x,z)$, is mapped onto the discrete colour bar symmetrically from –120 s^{-1} to 120 s^{-1}.

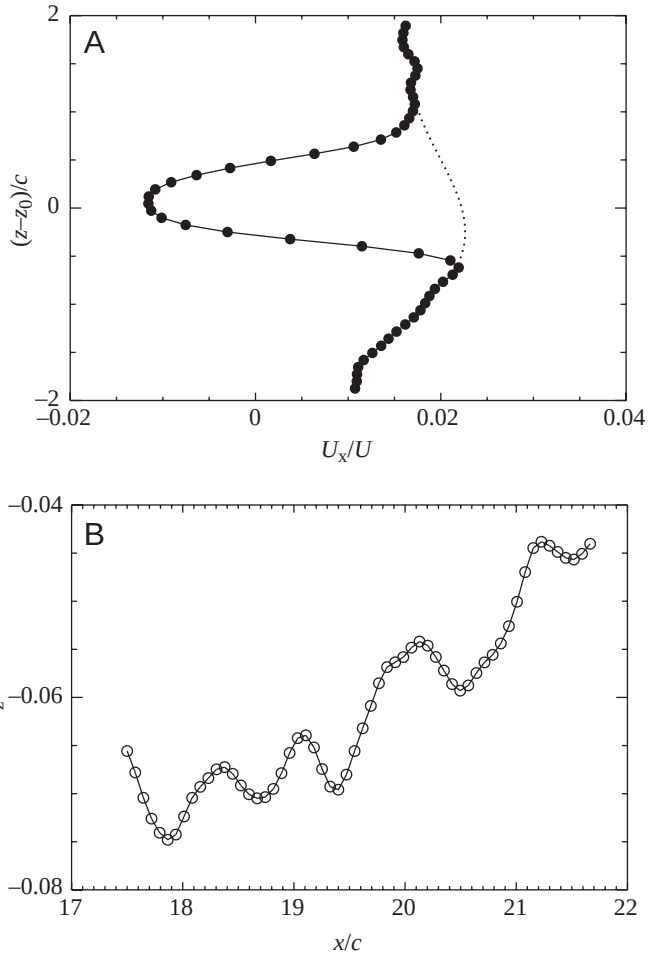

Fig. 19. (A) The mean streamwise velocity as a function of vertical distance from the wake centre. The dotted line is a polynomial interpolation for estimating the integrated drag of the defect profile. The peak defect value, U_x/U≈0.01, is about one order of magnitude smaller than typical centreline downwash velocities in flapping flight at this speed. (B) Mean vertical velocity distribution with streamwise direction. The downstream coordinate, x, has its origin at the estimated bird position, approximately 17 chords upstream of the data plane. See text for further details.

lines) approach each other, mostly due to a small decrease in the Ω^+. By contrast, recall that in the individual sequences of Fig. 12, the procession from wing root to wingtip was accompanied by an increase in Γ^-. Each individual result is rather sensitive to details of the cross-sectional geometry of the vortices and the resulting fraction that contributes to Γ^-. In Fig. 12, based on Figs 8 and 11, all of the stopping vortex was included in the calculation of Γ^-. The problem of correctly accounting for Γ that does not occupy a compact domain will be revisited shortly.

The three main results from Fig. 22 are that: (i) a closed vortex loop wake with even the highest measured circulation in the vertical centreplane would be unable to support the weight of the bird. The average fraction of weight support provided in this model is 45%. (ii) Significantly higher circulations (Γ^+, Γ^-) are not measured at more distal vertical planes, providing no evidence for any other simple candidate vortex topology. (iii) Ω^- and Γ^- are significantly beneath Ω^+ and Γ^+ and so a significant asymmetry is not accounted for by a simple closed-loop model.

A similar survey for the medium-speed (U=7 m s^{-1}) case is given in Fig. 23 (note the rescaled abscissa). While there are

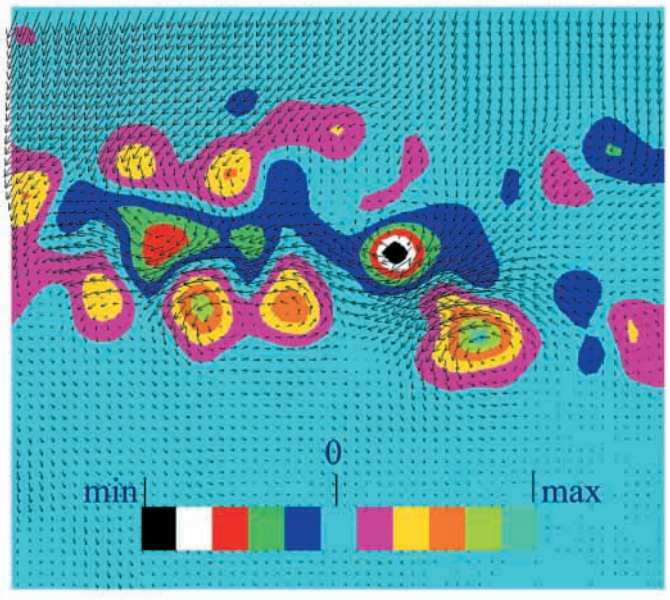

Fig. 20. Drag wake due to control manoeuvre in unsteady flight. The colour bar is symmetric, with extremes at $\omega_y(x,z)=\pm 200\ s^{-1}$.

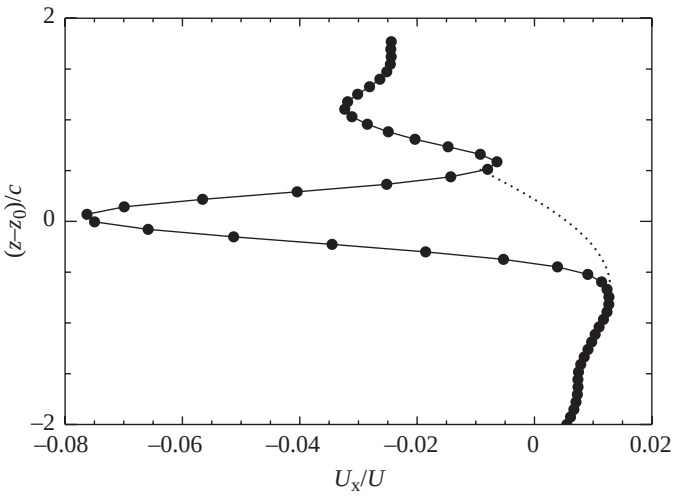

Fig. 21. Mean wake defect from Fig. 20. The dotted line is a polynomial interpolated baseline for drag estimates. See text for further details.

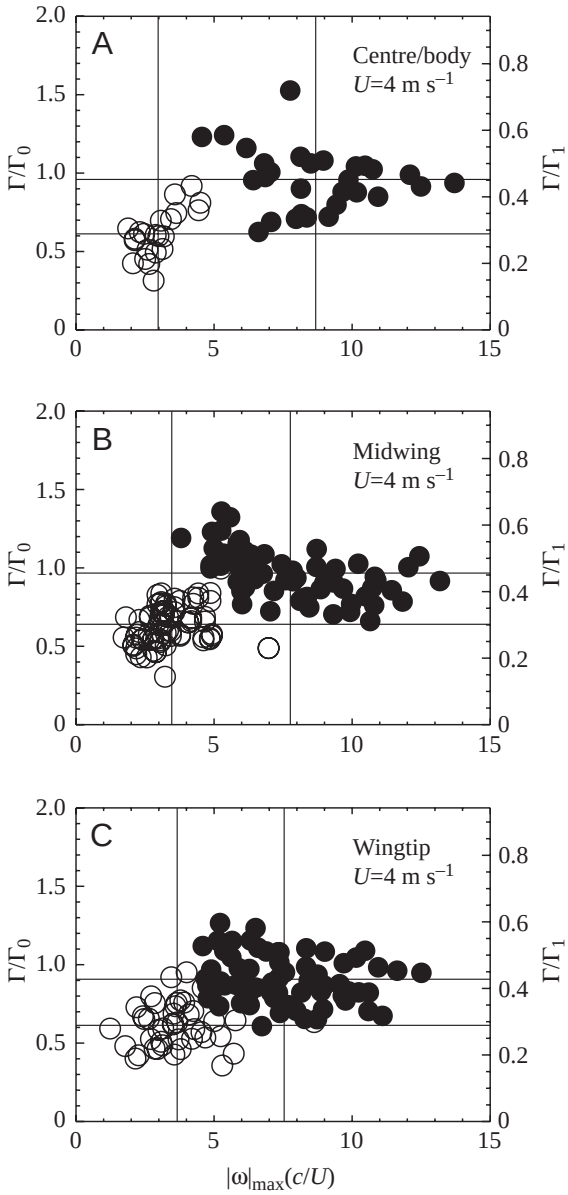

Fig. 22. Normalised circulations and peak spanwise vorticity for positive (filled circles) and negative (open circles) patches of vorticity in the slow-speed (U=4 m s^{-1}) wake at the centre/body (A), midwing (B) and wingtip (C). (The absolute value of the negative quantities is actually plotted here, and in most subsequent figures.) The solid horizontal and vertical lines are drawn at the average values, and their intersection approximately marks the centroid of the cluster of points. See text for further details.

differences in $\Omega^{+,-}$ and $\Gamma^{+,-}$ at the centre/body plane, they are much smaller than at the slow flight speed, and Γ^{+}, in particular is clustered much more closely around the mean value. At the midwing (Fig. 23B), the mean values of $\bar{\Gamma}^{+}$ and $\bar{\Gamma}^{-}$ are experimentally indistinguishable, a situation that continues on into the wingtip section (Fig. 23C). In all cases, however, $\Gamma/\Gamma_0 \approx 1$ and so $\Gamma/\Gamma_1 \approx 0.5$.

The insufficiency of plausible vortex loops with the measured Γ is less worrisome than in the low-speed case because the qualitative wake reconstructions (Fig. 15) have already shown the presence of a significant upstroke component. Nevertheless, while Γ/Γ_1 might be expected to be less than one, values of 0.5 or less might significantly complicate later attempts at calculating force balances.

Fig. 24 shows a different picture again at high-speed (U=10 m s^{-1}). In the qualitative reconstructions, the difficulty in finding identifiable concentrations of spanwise vorticity in the centreplane has already been noted (Fig. 16). Consequently, Fig. 24A has only two data points of either sign at the centreplane. It is quite likely that these represent slices toward the outer boundary of the region considered to be centre/body, but there is no manual editing of the data and so they must stand as given. $\Omega^{+,-}$ and $\Gamma^{+,-}$ at the centreplane have equal magnitude, and both rise at midwing (Fig. 24B). A straight-line wake composed of such vortices would more than

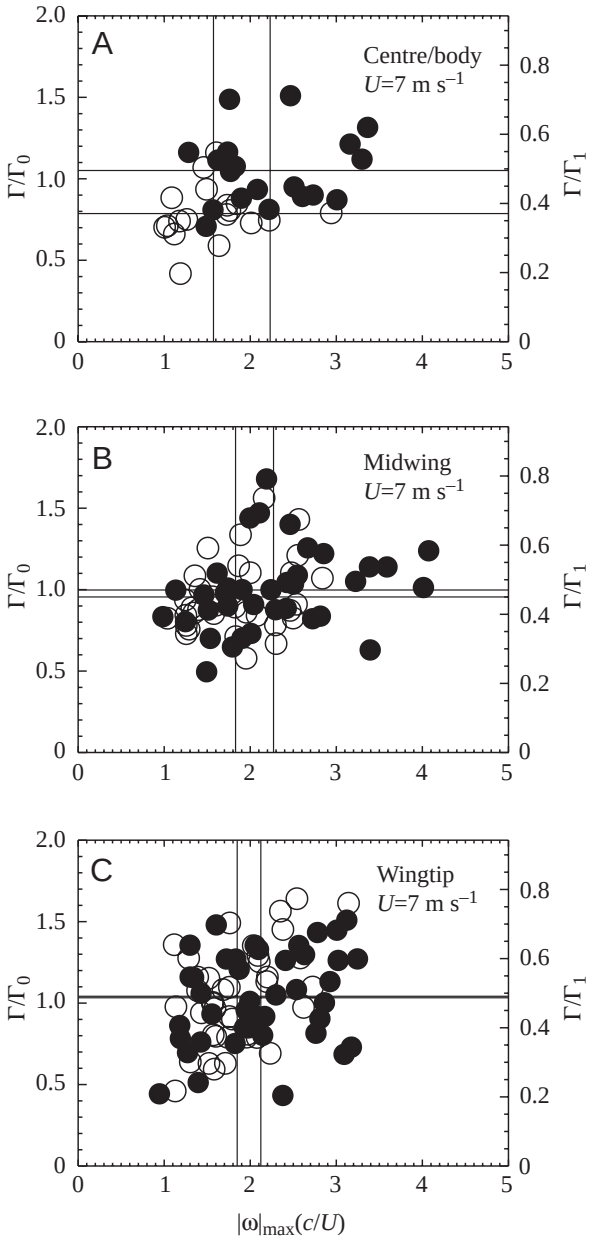

Fig. 23. As Fig. 22, but for medium-speed flight at 7 m s^{-1}. Note that the normalised $|\omega|_{max}$ scale goes only to 5 (one third of the previous figure).

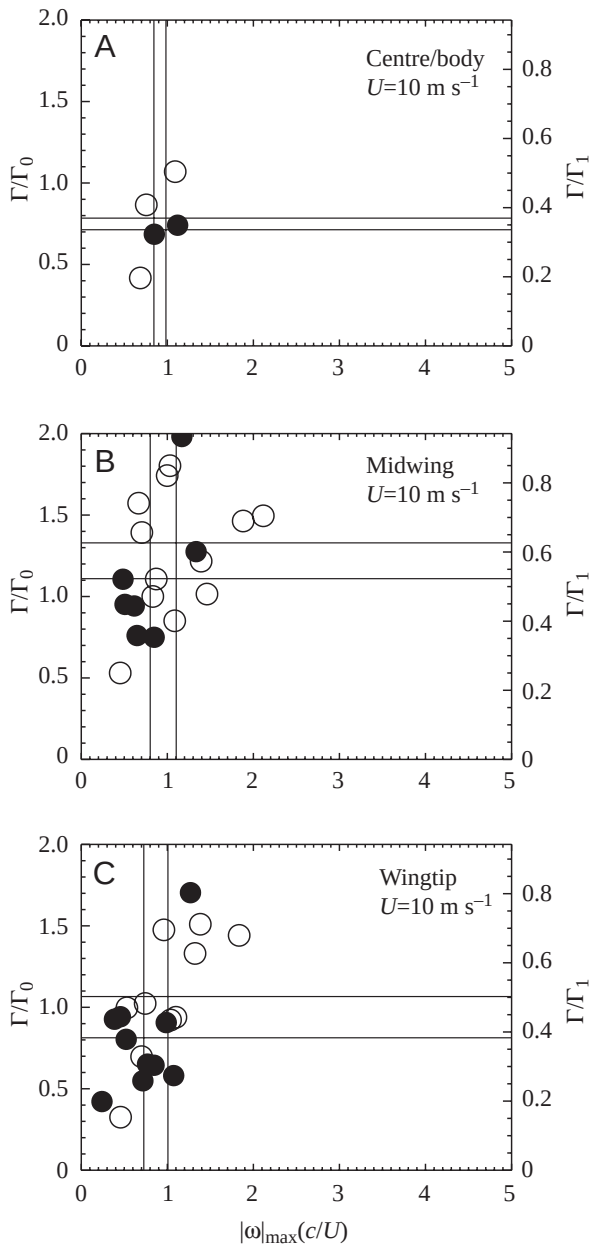

Fig. 24. As Fig. 23, but with a further 3 m s^{-1} increment in U for high-speed flight at 10 m s^{-1}.

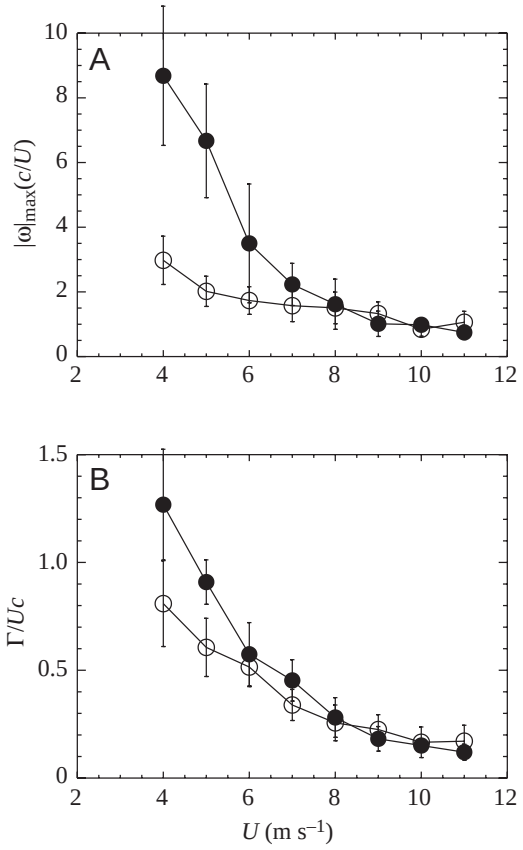

Fig. 25. The variation in peak vorticity magnitude $|\omega|_{max}$ (A) and total measured circulation Γ (B), rescaled by the wing chord c and mean speed U, for starting (filled circles) and stopping vortices (open circles) as a function of forward flight speed U.

balance the weight. The values of Ω and Γ both fall slightly towards the wingtip (Fig. 24C), but here the measurement is mainly dominated by flow instabilities of the trailing vortices themselves (Fig. 16E,F) whose magnitude is difficult to relate to the strength of the main vortex structure, where the primary component is now streamwise (ω_x), and most readily measured at the midwing section (Fig. 16C,D).

Continuous variations in peak and integrated vorticity magnitudes over the range of flight speeds

The choice of the three flight speeds covered in Figs 22–24 does not indicate anything particular about those speeds, and the same measurements have been made at all flight speeds in 1 m s^{-1} increments between 4 and 11 m s^{-1}. The mean and standard deviations of Ω and Γ for all measured flight speeds are shown in Fig. 25. At the lowest flight speeds, $\bar{\Omega}^{+,-}$ is strongly asymmetric, as is $\bar{\Gamma}^{+,-}$, though less noticeably (mirroring the result in Fig. 22). As U increases, the absolute value and asymmetry in both measures decrease. They do so gradually, without any discontinuities or abrupt changes. Γ and Ω fall with increasing U for the same reason they do in fixed-wing airplanes, as reflected in Equation 12, because the wake area per unit time available for weight support increases.

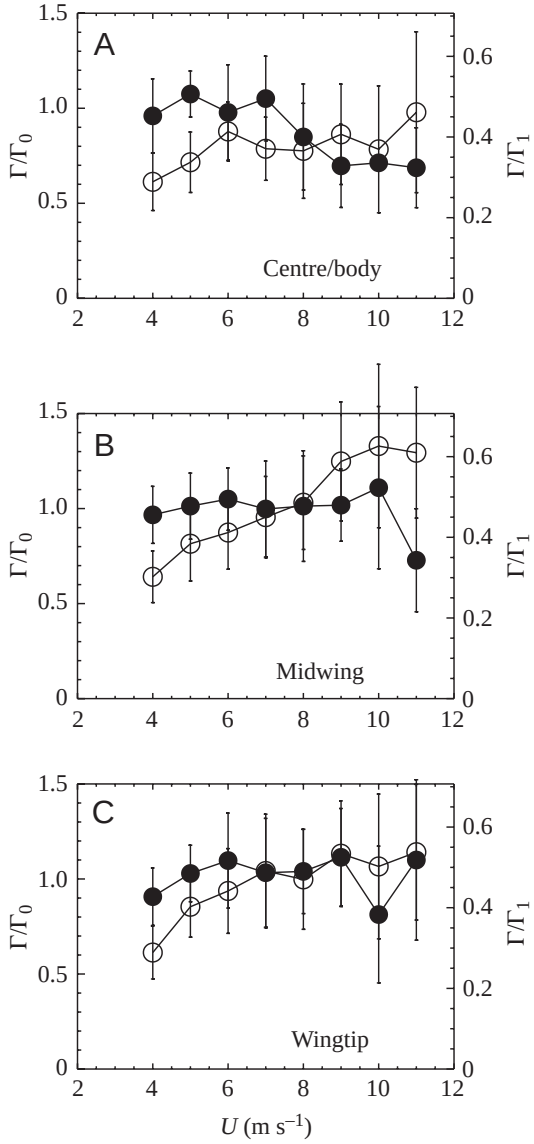

Fig. 26. Normalised circulations Γ of starting and stopping vortices over all U values and at three different spanwise locations: (A) centre/body, (B) midwing, (C) wingtip. The circulations are normalised by reference values that would be required for weight support at each U for wakes comprising constant-circulation straight-lines (Γ_0), and discrete, closed loops (Γ_1). The ratio between Γ_0 and Γ_1 depends on the downstroke ratio τ (as explained in the text), which is assumed to be held constant for this plot. Values are means ± S.D.

The asymmetry in strengths and shapes of vortex patches complicates estimates of the rate of wake momentum generation, but the main points can be illustrated with quite conservative assumptions. We again make use of the convenient reference values Γ_0 and Γ_1, the approximate circulations required for weight support if the wake were composed of straight line trailing vortices (Γ_0) or isolated ellipses (Γ_1).

Fig. 26 summarises the variation in the strength of the starting and stopping vortices at the three different span

locations. Beginning at the centreline data (Fig. 26A), one can immediately observe that, at slow speeds, despite the fact that the starting vortex is significantly stronger than the stopping vortex, if the wake were composed of elliptical vortex loops of this (highest) measured value, it would still only provide about half the impulse required for weight support over one wingbeat. While Γ/Γ_1 is only approximately 0.5, Γ/Γ_0 is therefore (Equation 20) approximately 1.0, but the best approximation of the wake structure at slow speed was isolated loops and certainly not continuous trailing vortices.

As U increases, the loop model becomes less and less appropriate, and one may then refer to values of Γ/Γ_0. At the centreline, these always fall short of 1.0, but this is to be expected as the vertical centreplane is the worst place, in principle, to measure a wake composed primarily of streamwise (not spanwise) vorticity. Thus, at higher speeds, one looks to more distal planes, such as the midwing (Fig. 26B) where reasonable cross-sections through curved trailing vortices are found. Indeed, Γ/Γ_0 values here are generally equal to, or above 1.0. The stopping vortex strengths are, if anything, higher than those of the starting vortices. They are both stronger here than at the centreplane, requiring/implying the existence of a significant streamwise component. This is completely consistent with the qualitative reconstructions of the previous section, which also argued for the existence of streamwise vortices continuing on into an aerodynamically active upstroke.

Of course, the constant circulation wake provides a smaller vertical projected area than the idealised rectangular wake, and so the circulation requirement will be higher than Γ_0, but not by huge amounts. The measured circulations for the gliding and flapping wake of the kestrel in Spedding (1987a,b) were 0.5 and 0.55 $m^2\ s^{-1}$ respectively. The rather small (10%) difference is partly due to the slightly larger lateral spreading of the wake on the downstroke of the flapping flight wake. Here too, it is likely that the wake width (which cannot be directly measured here with any useful accuracy) is (i) slightly increased and (ii) has increased in the time elapsed between generation and measurement. This time is always greater than T, the stroke period (recall Equation 4 and the related discussion).

The situation is quite similar at the wingtip (Fig. 26C). At higher speeds, Γ/Γ_0 is close to, or slightly above 1.0, and accounting for sufficient vertical momentum generation in the wake seems unlikely to be problematic. (A slightly more refined calculation will follow.)

For $U \leq 7$ m s^{-1}, the absolute value and relative magnitudes of starting and stopping vortices are similar at all spanwise locations. Unlike the case at higher speeds, there is no implication of other strong concentrations of vorticity, for example, in different orientations. The diffuse and relatively weak stopping vortex is just as diffuse and relatively weak at the wingtip as it is at the centreline.

A complete accounting of the measured circulation distributions

In trying to account for the shortfall in momentum of the slow speed wakes, the existence of some other topology than the ones emerging from the current reconstructions is unlikely. However, when the patches of vorticity are as incoherent and diffuse as they are in the stopping vortices, it is very possible that only some fraction of the total circulation is being correctly accounted for (recall Equations 6–8). Fig. 27 shows the results of a much less selective approach where all values of $\omega_y(x,z)$ of either sign above the usual threshold of 20% of the local maximum value are added toward the total circulation of that sign Γ_{tot}. (This amounts to adding up all the vorticity of the same sign as the peak vortex in each of the panels A–D of Fig. 6.) Integrating small values of the vorticity over large areas must be done with caution, as it would be quite easy to

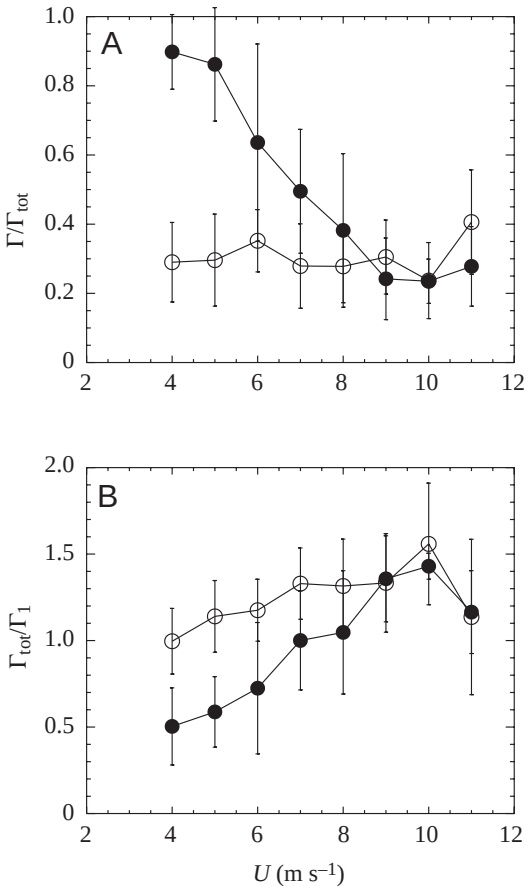

Fig. 27. Total integrated circulation Γ_{tot} from all positive (filled circles) and negative (open circles) vorticity in the observation window, plotted as a function of flight speed U. Although no single window contains the entire wake structure, each selected window, centered on peak values of either sign, contains all of the vorticity shed either at the beginning of the downstroke, or at the end of the downstroke and beginning of the upstroke. (A) The fraction of the total circulation that is not contained in the strongest vortex cross-section is very much higher in the stopping (negative) vortices than in the starting (positive) vortices. (B) The total negative vorticity would be sufficient for weight support, but not the positive component. The sum of the two, which ought to be zero (recall the convention of plotting the absolute value of the negative components), is not.

accumulate an area-dependent sum that is mostly measurement error. The conservative 20% threshold criterion avoids this problem since there are no errors of such magnitude. Moreover, in each case a quiescent patch of background is chosen and summed using the same criteria over a small area. This is then rescaled and subtracted from the grand total so that if any background noise did contribute to the total, then its average value would be subtracted out again. The magnitude of this correction was usually exactly zero, and always less than 1% of the total, when it could be traced back to difficulties in finding a truly quiescent patch in the vorticity field.

In Fig. 27A, Γ/Γ_{tot} for the starting vortices starts at values very close to one at slow flight speeds (4 and 5 m s^{-1}), and then drops continuously to just above 0.2 at the higher speeds. At lower *U*, there are no significant concentrations of positive vorticity other than the single, highest amplitude structure. That is not the case for the stopping vortices in the same figure. Here, they never account for much more than one third of the total circulation of that sign. Significant amounts of the total circulation of negative sign are unaccounted for by concentrating only on one structure. That being the case, then we might conduct a hypothetical case where at slow speeds the vortex loops are imagined to have started with a uniform circulation equal to the strength of the total circulation in the wake. The ratio of Γ_{tot}/Γ_1 will therefore be equal to 1.0 if such an accounting procedure would support the weight. It is shown as a function of flight speed in Fig. 27B. The total negative-signed circulation would have been sufficient for weight support, if at one time it were a good measure of the uniform circulation in an elliptical loop with the expected geometry, one produced every downstroke.

Now the problem is that the relation,

$$\Gamma^{+}_{tot} + \Gamma^{-}_{tot} = 0 \,,$$

which ought to be the case in a suitably defined control volume about a moving body or its wake, is not satisfied. The difference is large – about the same as the magnitude of the original wake momentum deficit. At first, this result seemed as if it might be an artefact of the different absolute thresholds of the vorticity magnitude, which in turn is a consequence of a fixed percentage threshold in each calculation. The entire calculation for Γ^{+}_{tot} was repeated using thresholds based on the magnitude of $|\omega^{-}|_{max}$ (rather than $|\omega^{+}|_{max}$). There was almost no difference in the Γ^{+}_{tot} results of Fig. 27B. This means that there is a real difference, independent of any particular thresholding procedure, between total positive and negative measured circulations. The positive-signed component occurs in very compact vortex cross-sections, whose total integrated magnitude is almost independent of very different threshold assumptions. The negative-signed contribution, on the other hand, is much more broadly distributed, yet has a higher total value, and no single vortex cross-section accounts for more than about 1/3rd of the total. The discrepancy is a low-speed phenomenon.

Where has the circulation gone? The answer is contained in the reconstructions of $\omega_y(x,z)$ shown in Figs 6 and 8. Careful inspection of that part of the vorticity field attributed to the upstroke shows that this domain contains regions of Γ^{+} as well as Γ^{-}. (Look carefully at Fig. 6A,C where white arrows show low amplitude, positive vorticity peaks, and also the middle of Fig. 8.) Now recall the accounting procedure for counting the sums of each signed patch of vorticity towards the total circulation (Equation 6). If the data includes a complete starting or stopping vortex structure, then the peak value is found and all circulation of that sign is eventually accounted for, but in that partial view of the wake only. The assumption is that the sections containing either starting or stopping vortices will have exclusively and solely vorticity of that sign. Any positive-signed patches that appear in predominantly upstroke-generated motions will be omitted. Similarly, any negative patches around starting vortices will be left out. In practice there are few of the latter, but the same is not true of the former, and while rather careful attention has been paid to correctly including all of the diffuse patterns of negative vorticity, the similarly scattered positive patches occurring in the wake regions categorised as upstroke have effectively been ignored. The pertinent parts of Figs 6 and 8 show that this contribution should not be assumed to be negligible, and the calculation procedure must be adjusted accordingly, one more time.

Fig. 28 shows a revised calculation of Γ_{tot}/Γ_1. Γ^{-} is calculated as before, but the estimate of Γ^{+} now includes the contributions from sections centred at both starting vortices and stopping vortices. Γ_{tot}/Γ_1 is never experimentally less than 1.0, for calculations based on total circulations of either sign, which, in turn, do not differ from each other. Sufficient circulation has been detected in the wake, so that if it is

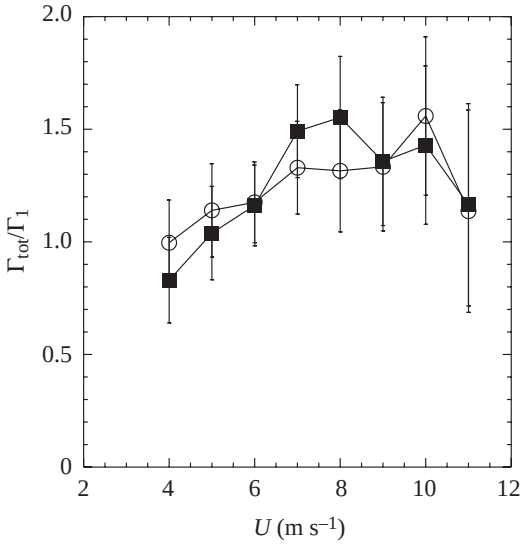

Fig. 28. As Fig. 27B, but Γ^{+} (filled squares) now includes all traces of above-threshold positive vorticity found in the neighbourhoods of the predominantly negative signed vorticity. Neither component is significantly different from the other (the sums balance), and both are within experimental uncertainty of sufficiency for weight support ($\Gamma_{tot}=\Gamma_1$).

assumed to have come from some initially coherent closed-loop structure with approximately uniform circulation of that magnitude, then this would be sufficient for steady level flight. This balance is only achieved if we include positive vorticity apparently shed towards the end of the downstroke and/or the beginning of the upstroke. The interaction of this opposite-signed vorticity with the mostly negative-signed patches shed at the end of the downstroke might account for the diffuse and incoherent distribution of the stopping vortices at low speeds.

Spanwise variation

One of the implications of this result is that the measured changes in circulation in the wake towards the end of the downstroke and beginning of the upstroke entail changes in circulation on the wing, which in turn imply translational or rotational acceleration. These changes may be uniform along the span, or local. The variation in measured $|\omega_y|_{max}$ and $\Gamma^{+,-}$ with spanwise location might provide evidence for local shedding, but no strong variation of the average values was shown in Fig. 12 for the 4 m s^{-1} case, other than the noted increase in $\overline{\Gamma}^{-}$ towards the wingtip. The data for spanwise variation in $\Omega^{+,-}$ and $\Gamma^{+,-}$ for all flight speeds are summarised in Fig. 29.

Although the effect does not fall outside the error bars, at low flight speeds the peak positive vorticity decreases systematically from the centreline outward to the wingtip (Fig. 29A), while the trend is reversed for the negative vorticity peak. Both trends gradually disappear at higher flight speeds (e.g. $U \geq 7$ m s^{-1}). At the same time, the circulations do not differ measurably or systematically from centreplane to wingtip (Fig. 29B) over any range of U. The simple interpretation of the flight model of Fig. 15 is fully consistent with both observations, as the same total circulation is spread out amongst an increasingly diffuse collection of vortex lines as the wingbeat progresses from beginning to end of downstroke.

There is some tendency discernable in Fig. 29 for a reduction in relative magnitude of the centreline circulation values at higher flight speeds, which is better shown in Fig. 30, where Γ is normalised according to the reference value for weight support in the rectangular (gliding) wake. At higher flight speeds, the centreline value is less than 1.0, and less than the values at more distal sections. Again, this is exactly what one would expect for a simplified wake model (such as Fig. 17) of primarily streamwise vorticity, which curves to intersect the data plane much more reliably and prominently towards the wingtips, where the streamwise vortices are presumed to originate.

The low-, medium- and high-speed wake topologies that are consistent with the qualitative and quantitative arguments thus far are summarised in Fig. 31. While these simple models based on the thrush nightingale data are incomplete in some details, the successful approximate accounting for the wake

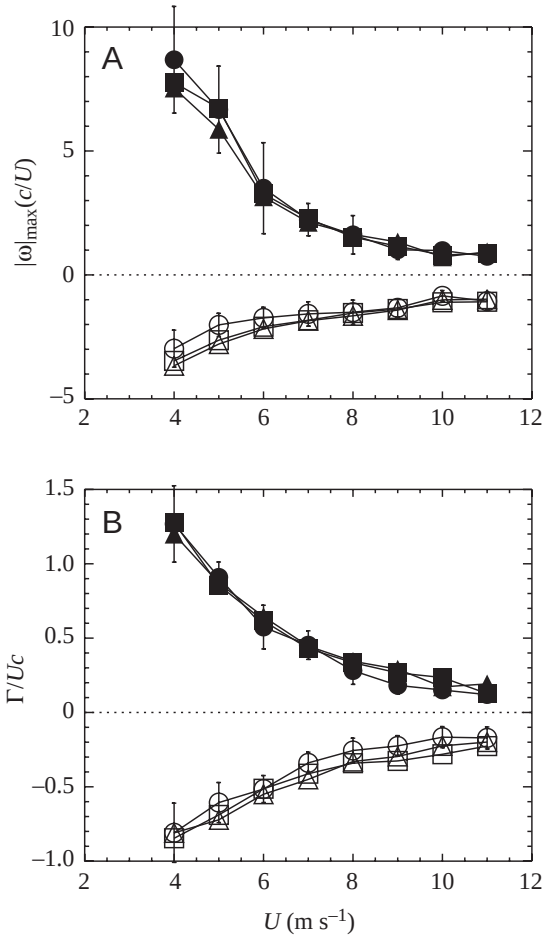

Fig. 29. (A) The variation in peak vorticity magnitude $|\omega|_{max}$, rescaled by the wing chord c and mean speed U, with flight speed U for positive (starting) vortices (closed symbols) and negative (stopping) vortices (open symbols) for three different spanwise locations: centreplane (circles), midwing (squares) and wingtip (triangles). (B) Same plotting conventions for the circulation of the patch of vorticity associated with $|\omega|_{max}$. Values are means, and ± S.D. are shown for the centreplane values only.

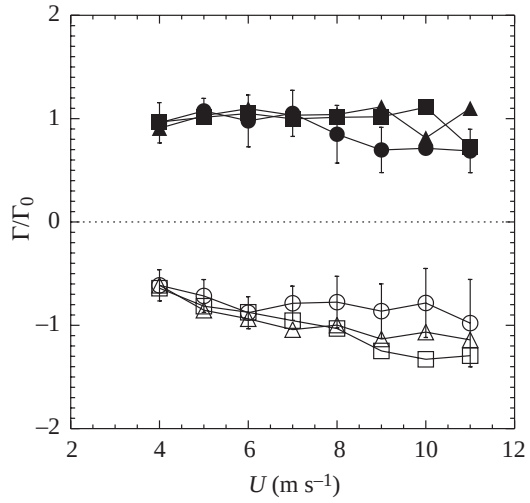

Fig. 30. The variation in normalised circulation Γ as a function of flight speed U and spanwise location. Symbols as in Fig. 29.

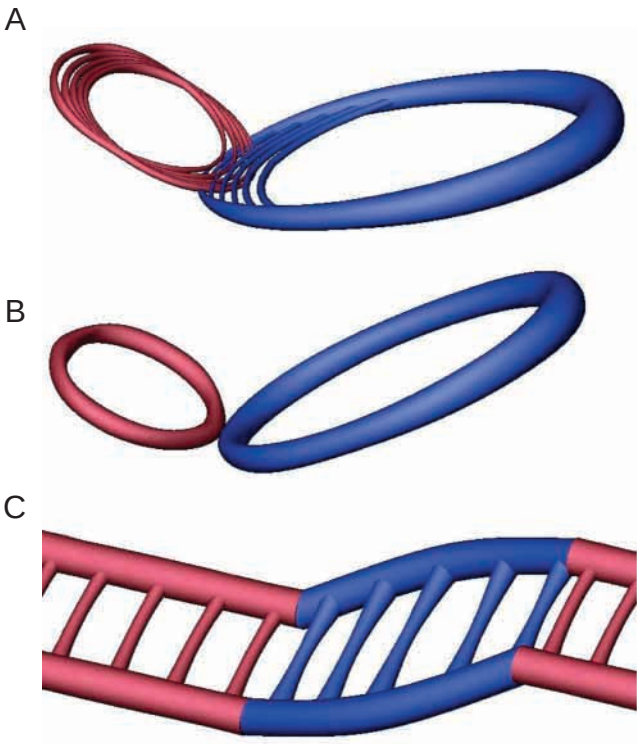

Fig. 31. A summary of three wake patterns deduced from vertical slice data at slow (A), medium (B) and high (C) speeds, respectively. The wakes are shown deliberately idealised and simplified to suggest the most important elements of a wake-based model. The three samples do not represent discrete wake topologies, and the transition from one to another is gradual, largely through changes in the vorticity shed during the upstroke. The tubes represent surfaces of constant vorticity magnitude, and are coloured blue or red according to whether they originated with down- or upstroke. The wakes have been rescaled to occupy approximately the same (streamwise, x) length on the page. In practice, the high-speed pattern at $11\,m\,s^{-1}$ has a streamwise extent of almost 3 times that of the low-speed wake at $4\,m\,s^{-1}$. (Many thanks to Michael Poole for this figure.)

momentum flux at all flight speeds supports the idea that the basic patterns are correct, and might be used as a basis for constructing, admittedly simplified, analytical and predictive models.

Discussion

A family of vortex wakes

Closed vortex loops to continuous trailing vortices

The qualitative and quantitative descriptions of the closed-vortex-loop wakes at low flight speeds are very similar to those of previous investigations. Not only that, but the aspects of the wake that differ measurably from simple closed-loop models are too. The diffuse and weak stopping vortex has been noted in both pigeon and jackdaw flight studies (Spedding et al., 1984; Spedding, 1986), and is seen here also. At low flight speeds, the cross-sections through starting vortices show quite a concentrated core structure (Figs 9, 10). In Fig. 10, the core radius can be estimated to be approximately r_0=1 cm for a nominal ring radius of approximately 9 cm (Fig. 8). The ratio, $r_0/r \cong 0.1$ is slightly smaller than previously measured values for slow flying birds (pigeon: 0.17±0.04, jackdaw: 0.14±0.03; Spedding et al., 1984, Spedding, 1986), but similar to that found in the medium-speed kestrel wake (downstroke: 0.1, upstroke: 0.4; Spedding, 1987b). The relatively small core size makes it reasonable to imagine adequate wake models that have a small number of concentrated vortex lines and also, if it is correct to speak of a ring, then the ring would qualify as small-cored (see Saffman, 1992, chapter 10; also chapter 13 for effects of viscosity).

As U increases, the distribution of vorticity in vertical streamwise planes becomes more complicated (Fig. 14). The strength of cross-stream starting vortices gradually decreases, and the relative contribution of the upstroke gradually increases. Finally, at the higher speeds, the centreline vorticity distributions, rescaled locally on the usual colour bar, show a broad spectrum of variations throughout the wingbeat (Fig. 16). The amplitudes are significantly diminished, however (Fig. 25). It is not clear whether previous experiments were unable to distinguish these relatively low-amplitude spatial variations in the velocity field, or whether the thrush nightingale is less proficient at constant-circulation wake generation than the kestrel, which is the only other point of quantitative comparison.

Perhaps the nearest points of theoretical comparison for these gradually varying wakes with complex cross-stream vorticity distribution are the wake circulation distributions predicted by the optimisation models of Hall and Hall (1996) and Hall et al. (1998), who numerically solved a variational problem to find the optimum (in the sense of minimum induced drag) spanwise, time-varying circulation distribution for rigid wings in both low- and high-amplitude flapping flight. A series of vertical cuts through their $\{x,y\}$-wake distributions of iso-circulation contours (fig. 13 in Hall and Hall, 1996) might be difficult in practice to distinguish from the result of the same operation on the empirical models of Fig. 31. There are two factors that complicate direct comparisons. First, the wake in Hall and Hall's formulation is assumed to be left at the trace of the wingtip trailing edge, without roll-up. While corrections to the computed optimal circulation distribution due to wake roll-up might be small, the experimentally measured wakes have rolled up and, particularly at low flight speeds, have had plenty of time to do so. As Hall and Hall point out, there is then no obvious way to infer the original circulation distribution on the wing from the rolled up late wake. For the same reason, the late wake would not be expected to have the same distribution of vorticity as the theoretical one, and the significance of observed differences is not clear. The second point is that rigid wings do not have the characteristic upstroke flexion that leads to the wake asymmetry required for positive thrust. Instead, the variations in spanwise circulation distribution move inboard. The net result is equivalent, with a net positive thrust, but one is achieved by varying the span of a wing with relatively constant circulation on the remaining reduced span (or so the

constant circulation model holds), while the other involves a spanwise variation of the circulation itself. Future quantitative tests against appropriately modified formulations of these analytical/numerical models would be very interesting.

In summary, while the low and high-speed wakes are not inconsistent with previous closed-loop and constant-circulation models respectively, most wakes (at most speeds) are not exclusively of either kind, but have some intermediate structure, with amplitudes of cross-stream vorticity at the centreline that decay gradually as U increases. The three examples of U=4, 7 and 10 m s^{-1} in Figs 8, 14 and 16 (and in idealised summaries in Fig. 31) are simply examples on a continuum whose gradually varying quantitative properties are summarised in Fig. 25. Since most bird flight models assume either closed-loop or constant-circulation wakes, then most models are inapplicable to most flight speeds encountered here.

No evidence for gaits

Until now, the only two previous structures discovered in bird wakes indeed appeared to be either some kind of closed loop or a pair of continuous trailing vortices. This has led to speculation about the possible existence of two (and only two) distinct gaits in bird flight (e.g. Rayner et al., 1986; Rayner and Gordon, 1998; Rayner, 2001), analogous, presumably, to the gaits encountered in terrestrial locomotion, and this notion has even spread to the more general literature (e.g. Alexander, 2002).

In terrestrial locomotion the changing balance of gravitational and inertial forces and spring forces in the muscles and tendons leads to distinct gaits such as the well-known walk–trot–gallop transitions in many quadrupeds (e.g. Hildebrand, 1965; Alexander, 1982), when the gaits can be distinguished in the differing phase relations and duty factors amongst the limbs involved. The notion of distinct gaits in terrestrial locomotion then involves quite abrupt transitions between them and also frequently involves the existence of forbidden speeds close to their margins.

In various studies of wingbeat kinematics (Tobalske and Dial, 1996; Tobalske, 2000; Hedrick et al., 2002), the absence of any detectable sharp transition in any measurable kinematic parameter has nevertheless been interpreted as marking a ‘gradual’ transition between ‘gaits’. In Hedrick et al. (2002), local changes in angle of incidence, α, and relative wind velocity, u_{rel}, were inferred from wing traces, and then converted through a presumed two-dimensional analytic relation of $C_{\mathrm{L}}(\alpha)$ to lift L, and thence by Equation 11 to estimates of Γ. Aside from the question as to whether local two-dimensional, steady, inviscid $C_{\mathrm{L}}(\alpha)$ relations can apply to the high-amplitude, three-dimensional unsteady flapping motions of the wings (particularly at low U), it is most likely that gradual changes in u_{rel} and α would lead to correspondingly gradual changes in Γ on the wing and in the wake. That is actually inconsistent with any gait selection mechanism, but fully consistent with the gradual variation in strengths of cross-stream vortex structures observed here.

No other study of bird or bat wakes, quantitative or qualitative, has involved more than two flight speeds. There is no indication, in any of the results in Figs 22–30, where numerous quantities are plotted as continuous functions of flight speed, that any sharp or discontinuous transition in wake topology occurs, at any U. Moreover, most of the wake topologies, at most flight speeds, are not closed loops or continuous vortices, but are some kind of intermediate form, where the strength of the cross-stream vorticity gradually decreases with increasing flight speed. In the case of the thrush nightingale, the notion of distinct gaits is not only non-useful, but it is qualitatively and quantitatively incorrect.

Since there are no other wake data covering a range of flight speeds, then the reasonable working hypothesis is that gradual transitions occur from low-speed to high-speed wakes of flying birds through gradual increases in cross-stream vorticity, much as originally hypothesised and discussed in Spedding (1981,1987b), Pennycuick (1988) and Spedding and DeLaurier (1996). We should point out, however, that the common intermediate wake structure is not quite as predicted by these authors. Instead of single connecting strands of vorticity representing decrements and increments of the circulation on the wing, the upstroke here sheds its own starting and stopping vortices, to form a double-ringed wake. The upstroke wake is more distinct at medium to low speeds. It forms the bridge between wakes with discrete elements at low speeds and continuous variations at high speed. The purportedly distinct closed-loop and constant-circulation wakes are otherwise simply single points on the continuous curve.

The wake momentum paradox

The problem

The wake momentum paradox arose because quantitative measurements of the wake in slow-flying pigeons (Spedding et al., 1984) and jackdaws (Spedding, 1986) produced at most 50% of the momentum required for weight support. The magnitude of the deficit greatly exceeded any reasonable uncertainty estimate of the wake measurements used in its calculation (primarily the diameter and circulation of the closed-loop structures). Using the same measurement and analysis techniques, there was no corresponding deficit for the medium-speed flight of either gliding or flapping kestrels (Spedding, 1987a,b). In the absence of further data in the intervening years, the conundrum has remained unsolved.

Although it has been suggested (Rayner, 1991b, 2001) that birds in very slow flight do not or cannot fly straight and level but are in fact decelerating at about 1/3 $\boldsymbol{g}$, there is solid evidence to the contrary. This includes experimental evidence from analysis of high-speed cine film (Spedding, 1981) of both pigeon and jackdaw flight under very similar circumstances to the original experiments, and from tracings of trajectories of the feet or eyeballs in the same multiple-flash photographs used for the original wake analysis (Spedding, 1986). The evidence also includes the practical difficulties that, for the particular experimental geometry, a ballistic trajectory of constant 1/3 $\boldsymbol{g}$ deceleration would require initial vertical speeds greater than

the horizontal flight speed, and that the birds did in fact arrive in front of the cameras with a very small net increase in height. The original statement of the problem should thus be taken at face value, and the low speed results continue to provide a puzzling context for this work.

The solution

The initial results in this study (Fig. 22) replicated and confirmed the original wake momentum paradox, with circulation values between 30–60% (Γ/Γ_1 in Fig. 22) of that required for weight support from planar vortex loops with the measured size. It became clear (Fig. 27) that a significant fraction of the total circulation could reside in low amplitude, diffuse patches of vorticity, and it was only when positive vorticity from the end of the downstroke part of the wake was included in the total (Fig. 28) that the sums finally added up, equally, to 1.0. The previous wake momentum deficit was caused by substantial amounts of circulation being effectively omitted from the calculations because it was (i) beneath the measurement resolution, and (ii) not in the expected place.

The bubble cloud method calculated the wake circulation by integrating in a straight line down the centreline of the ring-like wake structure (Spedding et al., 1984). Application of Stokes's theorem to fluid flows that can be represented by concentrated vortex lines or tubes embedded in an otherwise irrotational flow shows that any line integral around a closed path containing the vortex lines will converge to the same value of the circulation. However, the total circulation cannot be measured if the closed curve does not include all the vorticity. The straight line approximation presumes that all the vorticity of opposite signs lies either side of the dividing streamline. We now see that this is not the case, and so the previous technique was bound to underestimate the total wake circulation. Furthermore, the comparatively limited resolution of the bubble cloud method did not allow the other important but diffuse traces of vorticity to be distinguished. In this study, the initial measurements of the circulation in Fig. 26 effectively share the same assumptions, confining all the measurements to particular contiguous blobs, and that is why they show the same apparent momentum deficit. The deficit disappears when all the above-threshold vorticity, in its complex distribution, is properly taken into account.

The difficulty in using measured circulation values to deduce wake momentum generation rates in a real experiment should not come as a surprise, for three reasons. First, although making force estimates from wake surveys is a classical wind tunnel technique, in practice it requires careful measurement in tightly controlled conditions, and recent studies (Spedding et al., 2003; Spedding, 2003) have shown the non-negligible uncertainty in estimating drag (for example) from DPIV wake measurements behind even a simple fixed wing model geometry at Reynolds numbers and aspect ratios comparable to the bird flight experiments reported here. The measurement difficulties are compounded when the downstream measurement location, x/c, is far away, and when one is trying to exploit a simplified conceptual model of a complex generation mechanism. Both concerns apply here, particularly at low flight speeds.

The second point is that efficient locomotion of well-trained animals in a properly controlled experiment will probably not generate large excesses in momentum above that required for propulsion and weight support (if applicable). The more rigorous the experiment, the smaller will be the excess. The wake impulse to correctly balance the known (or presumed) body forces is therefore a maximum measurable quantity, and most measurement techniques will approach this value from below, erring on the low side. The story told by Figs 22–24, 27, 28, reveals how to do this for the family of wakes discovered for the thrush nightingale.

The third and final point concerning the likely difficulty in making momentum-balancing calculations in turbulent flows at moderate Reynolds number is that phenomena such as cancellation of vorticity and reconnection of vortex lines can significantly modify the qualitative and quantitative properties of fluid flows. Cantwell and Coles (1983) measured circulation deficits of up to 50% in moderate *Re* flows behind circular cylinders. The abrupt change in topology of neighbouring vortex structures through mutual interactions has been extensively investigated (e.g. Boratav et al., 1992; Zabusky et al., 1995) for initially parallel tubes and for orthogonal orientations. The fact that the sums eventually did balance in the bird wake could be used to argue that these dissipative interactions did not in fact occur (or rather that they were not significant in the overall energy budget), but the situation may not be so simple, and the crude accounting method where all circulation of either sign was lumped into simplified down- and upstroke structures may camouflage a more complex and intrinsically difficult problem. Luckily, this problem currently lies beneath the accuracy of our simple vortex-wake model reconstructions, and an approximate balancing of the forces can be considered to have been achieved. However, one may note that significantly improved measurement resolution in future studies might in fact uncover significantly harder wake measurement and force balance problems.

To the degree of accuracy that one might reasonably claim from these wind tunnel experiments, the momentum balance puzzle can be considered to be solved. Ultimately, the resolution of the long-standing wake momentum paradox was only possible because the new, customised data acquisition and analysis methods allowed estimates of the velocity field and its gradients with superior resolution in space and amplitude. It is not likely that any method that relies on tracking of individual bubbles, even if it is in three dimensions, will have such resolution. Finally, it is worth inspecting once again superimposed images of the velocity and vorticity fields such as Fig. 8. If the accurate calculation of $\omega_y(x,z)$ were not available, qualitative inspection of the velocity field alone would give no hint of the true complexity of its gradient field. Similarly, any conclusions that rely solely upon qualitative interpretation of even well-resolved velocity fields or bubble tracks have no chance of providing unambiguous information

about likely vortex wake structure, which can only be deduced with assistance from quantitative measurements.

High-lift mechanisms at low flight speeds?

The major contribution to previous shortfalls in wake momentum measurements seems to be related to shedding of positive vorticity in the latter part of the downstroke or early part of the upstroke. The source and significance of this are not known. If it indicates a commensurate temporary increase in circulation on the wing, this may be either some kind of high-lift mechanism using control of separated flows, or it may only mark a control adjustment whose effect is not noticeable until the beginning of the upstroke.

The continued immersion of the wings and body of slowly flying birds in the downstroke-generated wake has been noted before (Spedding, 1981, 1986) and is an inevitable consequence of the high reduced frequency at low flight speeds (Table 2), where the smallest fraction of a wingspan of forward travel is achieved with each wingbeat cycle ($\lambda/2b=UT/2b\cong1.1$ for $U=4$ m s^{-1}). One can expect not only body–wake interactions but also wake–wake interactions as the spacing between successive structures is small, or comparable to their size. Again there are two issues that may or may not be related. First, the various interference effects of body–wake and wake–wake interactions are very likely to disrupt any pre-existing orderly wake structure, making it more difficult to account for the both the energy and momentum when the wake is eventually measured, at least one wingbeat later. Second, there is the possibility that these interactions might be advantageous, either directly in increasing lift or reducing drag, or indirectly, in assisting flow control either through the appropriate positioning of wake structures or the maintenance of favourable pressure gradients.

An interaction between the wake vorticity and wing surface has been demonstrated by Dickinson et al. (1999) (see also fig. 4 in Yan et al., 2002) for mechanical model simulations of the hovering flight of the fruit fly. Intermittent, high-lift forces at the beginning of up- and down-strokes were measured and correlated with the wing section intersecting favourable induced flows from previous parts of the wingstroke. This phenomenon was termed ‘wake capture’, though it can also be viewed more generally as a strategic placement of the wing in a pre-existing, non-uniform flow field. In hovering flight, the reduced frequency, $k=2\pi fc/2U$, is infinite, and the hovering fruit fly and its model both sit directly on top of the pre-existing wake, increasing the likelihood of significant interactions. The Reynolds number is also significantly lower ($Re\approx10^2$) and the flow around and behind the wings is dominated by large vortices generated by boundary layer separation at the leading and/or trailing edge. It is possible that an analogue of wake capture occurs in bird flight at very low speeds, and that it both provides useful mechanical force and complicates the wake measurement. The existence and importance of strongly separated flows on bird wings at low flight speeds is currently a matter of conjecture, direct measurement being very difficult. The most promising approach will likely be adaptation of mechanical models to non-zero forward speeds and to geometries and Reynolds numbers approaching that of bird flight.

The footprints of gliding and control: quick estimates of horizontal and vertical momentum generation

The gliding and control wakes shown in Figs 18 and 20 help to interpret the usual steady flapping flight case by contrast. One aspect is to clarify the role and relative importance of the wake shed by the body alone. When a wake is measured continuously throughout the wingbeat, as in Figs 14 and 16 for moderate and high speeds, respectively, one might suspect that the effect of the body itself (rather than the wings) is being measured, especially in vertical centreplane cuts. To some extent this is necessarily true, as the body is treated as part of the wings whenever the wings are aerodynamically active. One cannot therefore distinguish between induced downwash due to wing loading or due to body loading since, to a first approximation, they are the same thing. The dominance of the wing-induced downwash can be clearly seen in the gliding wake of Fig. 18, superimposed on which is a relatively low-amplitude drag wake attributable to the body.

The interpretation would be considerably different if there were significantly different patterns of vortex shedding at the wing root than at the midwing, or if the peak vorticity (and circulation) magnitudes were different in the two locations. Fig. 14A,B shows this is not the case. Furthermore, the primary structures observed in Fig. 14A trace the up-and-down path of the wing and not the body, whose vertical excursions are very much smaller, and not in phase [data in Pennycuick et al. (2000) show the vertical body position leads the vertical wing position by 90°].

The mean wake profiles such as Fig. 19A can in principle be integrated to find the rate of change of momentum in x. The details can be found both in current textbooks (e.g. White, 2003) and the classics (a detailed account appears in Prandtl and Tietjens, 1934). Far downstream of the original disturbance, the pressure fluctuations can be neglected and the drag force can be estimated from

$$F_{\mathrm{D}} = \rho \int_{\mathrm{A}} u'^2 \, dA \,, \tag{21}$$

where A is the cross-sectional area (in $\{y,z\}$) over which a measurable wake defect velocity of u' can be measured. For a sufficiently large control volume (effective A), then the wake defect measured by Equation 21 would give the sum of the viscous and pressure drags around the wings and body. The profiles of $U_{\mathrm{X}}(z)$ are available in occasional single vertical planes only in this experiment, and direct estimates of the drag from Equation 21 are too sensitive to assumptions about being on the exact centreplane through profile cross-sections of uncertain shape to be useful for absolute values.

Nevertheless, comparative estimates can be made between the gliding and control cases. The mean velocity defect profiles of Figs 19A and 21 are both taken from the vertical

centreplane, behind the body, but with an uncertainty in y position of about 50% of a body diameter. If Equation 21 is applied to these profiles, using $U_X(z)$ as a measure of $u'(y,z)$ by assuming that the profile is circular in cross-section, then $F_{D,Control} \cong 2F_{D,Glide}$. The detectable difference shows that control manoeuvres can be detected and measured in the wake. Here a drag force of twice the usual body drag is used, presumably to adjust the x-position in the wind tunnel, moving further downstream from the perch and reference point. The adjustment to move in the other direction (upstream, back towards the reference marker) will not be observable in a directly comparable wake (same structure but mean positive defect), but as a flapping wake with stronger measured circulation. The calculations are approximate only, but they show the potential of the method for measurements of wake features from control or unsteady manoeuvres, and also for drag measurements in general.

There is strong interest in making correct estimates of total drag derived directly from the fluid motions, because the experimental estimation of frictional and profile drag coefficients of wings and bodies of animals, dead or alive, tethered or in free flight, is very difficult, even more so at Reynolds numbers typical of bird flight (Table 2), despite various ingenious experimental attempts to do it (e.g. Pennycuick, 1968b; Tucker, 1990a,b; Pennycuick et al., 1992, 1996). At the Reynolds numbers and aspect ratios in question, estimating drag even from the wake of a fixed wing by integrating wake profiles and calculating forms of Equation 21 is not as straightforward a procedure as it might first appear (Spedding et al., 2003; Spedding, 2003), because unsteady and three-dimensional effects are always present. Nevertheless it is possible, and further experiments are recommended in repeatable conditions designed to assure steady gliding (tilting the wind tunnel, for example) so that systematic profile surveys can be taken across the wake to include all contributions to the drag.

Equation 21 does not include contributions from the induced drag, which introduces terms with velocity components in the spanwise and vertical directions. However, there are yet simpler expressions for the vertical induced velocity of a finite lifting wing (see Prandtl and Tietjens, 1934). In the far wake, the induced vertical velocity, w_1, is twice the value on the wings themselves, and the lift force is the product of w_1 times the mass flux affected by the presence of the wings,

$$L = w_1 \rho U S' . \quad (22)$$

The equivalent cross-sectional area, S', depends on the velocity distribution on the wing and, in the case of the elliptically loaded wing, $S'=\pi b^2$, a circular wing disc area with diameter equal to the wingspan (it is indeed the same actuator disc described in the introduction). Because w_1 varies rather slowly with span, its estimation is quite robust (cf. estimates of u'), and the mean profile of $W_Z(x)$ in Fig. 19B gives an idea of the variation in averaged quantities. For a first estimate, let us approximate w_1 with the mean vertical velocity, $\overline{W}_z$, measured from Fig. 19B. Equation 22 then evaluates to L=0.5±0.2 N, and compares with a body weight of approximately 0.3 N. The uncertainty is large but the values overlap, and the vertical momentum generation rate is sufficient for weight support and consistent with classical wing theory.

Having shown that simple fixed-wing aerodynamic models can be applied without great problems to the appropriately selected data sets, we now consider a general model for the more complex flapping flight case, based on the measured bird wake data.

A simple flight model: the E–R wake

Here, we attempt to construct an empirical flight model. It is based specifically on the thrush nightingale data, but contains features that may be quite general. In this spirit, and given the difficulties in describing the precise wake geometry, the model need not be complicated and some quite broad assumptions can be allowed. A good starting point for a general model that can approximate the geometry and transitions in Fig. 31 might be the Ellipse–Rectangle (E–R) geometry, whose basic principles were originally introduced in Fig. 2B. Fig. 32 shows how the E–R model is constructed. The downstroke always sheds a wake covering an area described by an ellipse.

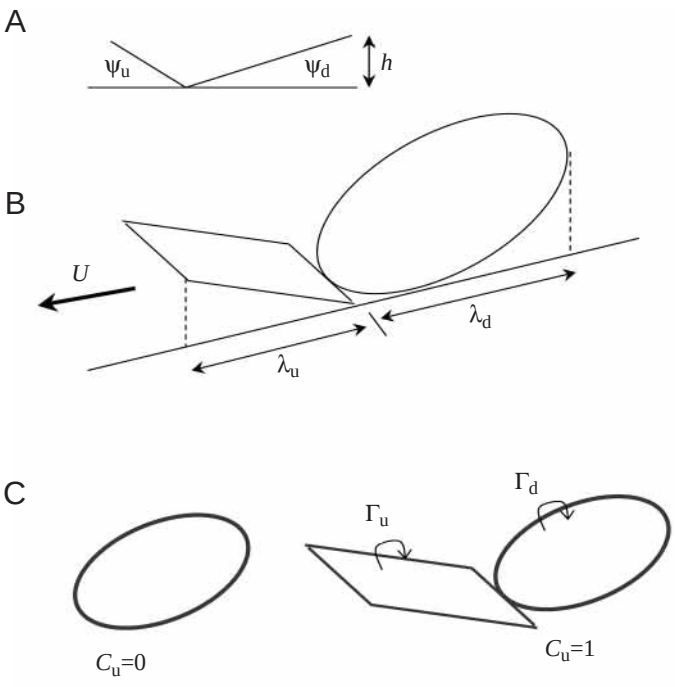

Fig. 32. (A) The Ellipse–Rectangle (E–R) wake is the simplest single model geometry that describes the wakes found over all flight speeds. Two planar wake areas are shed by the downstroke and upstroke, and they are elliptical and rectangular in shape, respectively (B). In order to calculate and test vertical forces, only the projections onto the horizontal plane need be considered. (C) A weighting function $C_u(U)$ varies between 0 and 1 from U_{min} to U_{max} to gradually change the relative contribution from the upstroke (rectangular) component. λ, wavelength; ψ, wake element inclination angle; τ, downstroke ratio; h, height. The d- and u-subscripts refer to down- and upstrokes.

The aspect ratio of this ellipse depends primarily on the forward speed, U, and the wingspan, $2b$. The upstroke always sheds a rectangular wake, with circulation that gradually increases from zero at the lowest flight speed, to equal to the downstroke circulation at the highest flight speed. The extremes (in U) of this model thus replicate simple analogues of the closed-loop and constant circulation wakes. Just as in the experiment, most wakes are of some intermediate form.

The vertical impulse of the two wake segments can be written:

$$I_{z,d} = \rho\pi b \left(\frac{\lambda_d}{2}\right)\Gamma_d$$

and

$$I_{z,u} = \rho 2bR\lambda_u\Gamma_u\,, \qquad (23)$$

where λ_d and λ_u are the horizontal wavelengths of the downstroke and upstroke wakes:

$$\lambda_d = UT\tau$$

and

$$\lambda_u = UT(1-\tau)\,, \qquad (24)$$

T is the wingbeat period and τ is the downstroke ratio, as previously defined.

Γ_d and Γ_u are the unknown circulations, whose values will be taken initially from experiment. The relative wake width in y is determined by the span ratio, R, which is a number less than 1.0 representing the projected relative span of the flexed wing in its upstroke position. The rather sparse data that exist (Spedding, 1987b) suggest that this can be approximated as constant. The current data at single vertical slices here do not help in improving the certainty of this estimate.

Now, the total vertical impulse is

$$I_z = I_{z,d} + I_{z,u}\,. \qquad (25)$$

It remains to measure or estimate Γ_d and Γ_u, a rather familiar problem by now. At low flight speeds, Γ_u is small, and the wake has been shown to be well represented by ellipses with constant circulation equal to the values described in Fig. 28. As U increases, so does the relative contribution of Γ_u, until Γ_u=Γ_d. The experimental data again suggest that the relation between Γ_u and Γ_d can be approximated by a simple monotonic function over all U. To simplify, Γ_u is set by

$$\Gamma_u = C_u\Gamma_d\,, \qquad (26)$$

where $C_u(U)$ is a continuous function between 0 and 1. To further simplify, it is set here to be linear. If estimates of $\Gamma_d(U)$ are available, then the average vertical force F_z over one wake period (which ought to equal the weight, W) can be calculated directly from

$$F_z = \frac{I_z}{T} = W\,. \qquad (27)$$

Similarly, the net horizontal force F_x can be calculated, in principle, from the difference in vertical projections of the two wake areas,

$$I_x = I_{x,d} - I_{x,u}, \qquad (28)$$

and these are once again completely determined by the assumed or measured kinematics and wake geometry, with only Γ_d and Γ_u as unknowns:

$$I_{x,d} = \rho\pi b \left(\frac{h}{2}\right)\Gamma_d$$

and

$$I_{x,u} = \rho 2bRh\Gamma_u\,. \qquad (29)$$

where h is the vertical wake height, as shown in Fig. 32, and R is span ratio. In steady flight, the horizontal impulse per unit time balances the drag D, which is the thrust F_x:

$$\frac{I_x}{T} = -D = F_x\,. \qquad (30)$$

In practice, D is much smaller than L, and would be poorly resolved by the crude model geometry. Moreover, practical resolution of the drag forces is much more complicated because it is the fluid itself that exerts the drag force in the first place. Thus in steady, unaccelerated forward motion the viscous drag wake is balanced by the increase in momentum of the opposite sense in the thrust wake, and in a suitably defined control volume (i.e. one that contains an integer number of wingbeat cycles) the net horizontal momentum will be exactly zero. This is true for all self-propelled wakes, be they from birds or aeroplanes, fish or submarines. One would only expect to be able to calculate either thrust or drag if the drag part of the wake were easily separable from the thrust part. The more complex the wake structure, the harder this will be.

It is not the purpose of the current exercise to devise a sophisticated or accurate model, but rather to test and demonstrate the self-consistency of the concept, using the simple criterion of sufficiency of weight support. It is quite instructive to follow the calculation of I_z, step-by-step, as illustrated in Fig. 33.

Fig. 33A shows the increase in projected horizontal wavelength with increase in flight speed, U. Since the wingbeat frequency changes little, the stride-length or advance ratio increases with U. It corresponds to a decrease in reduced frequency. Commensurately, if the wake height is assumed to be constant (this is not quite true, as indicated in Fig. 31, but at this level of detail the correction is unimportant), the angle to the horizontal of both upstroke and downstroke wake segments decreases with increasing U (Fig. 33B) and the horizontal projected area of each segment also increases. The projected area (Fig. 33C) is normalised by a wing disc area calculated from the wing semispan. At 6 m s^{-1}, the ratio of projected to disk area is approximately 1.0, and the bird progresses forward by about one wingspan per wingstroke (see also Fig. 33A).

Fig. 33D shows the measured circulations of the strongest single wake vortex (open circles) and total mean circulation of either sign (closed circles). At slow flight speeds, the best estimate of Γ for the wake is Γ_{tot}. With increasing U it becomes less appropriate because there is no good reason to suppose that the almost continuous shedding of small concentrations of vorticity can be simply lumped together as if there were one big wake structure. Instead a better estimate might now be Γ_v,

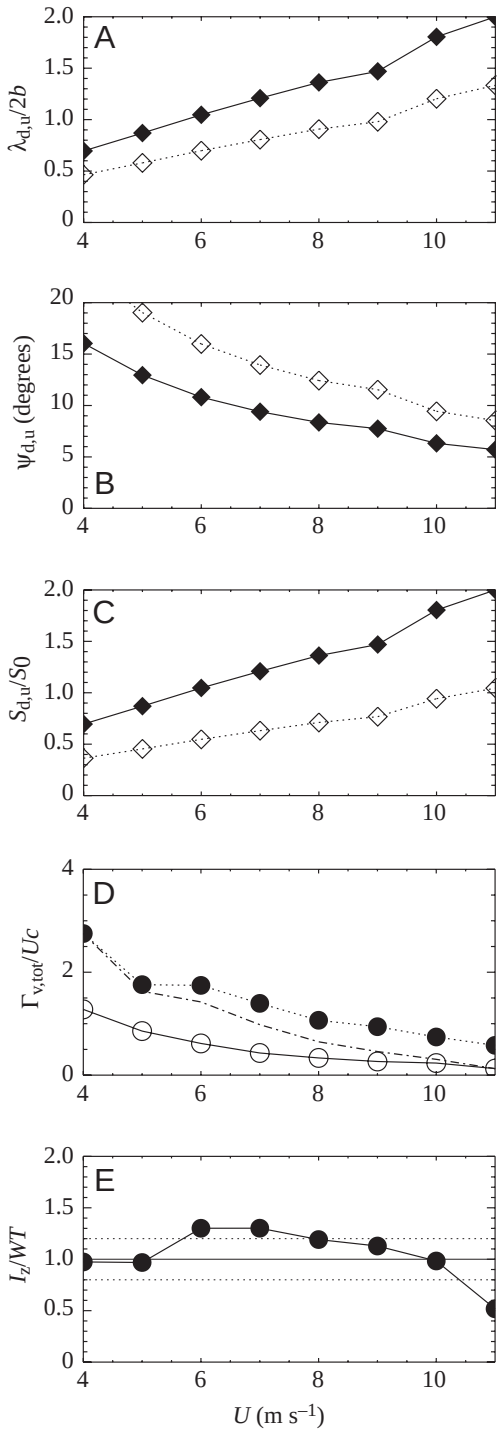

Fig. 33. Predicted/measured wake parameters for the thrush nightingale, and their contribution towards the total wake impulse. (A–C) show the horizontal wake length (λ, A), inclination angle (ψ, B) and projected area (*S*, C) for the downstroke (solid diamonds) and upstroke (open diamonds) segments. In (D), alternative estimates of the wake circulation are available from either the strongest measurable single vortex (Γ_v, open circles), or from the mean total circulation of either positive or negative patches of vorticity (Γ_{tot}, closed circles). Based on the wake reconstructions in this paper, and on the assumptions of the E–R model geometry, the best estimate comes from a weighted sum of the two, shown by the dash-dot line. In (E) the fraction of weight support provided by the wake model is plotted for all flight speeds. The magnitude of the error bars will be similar to those shown in Fig. 28. Thus all points lie within ±20% of one. I_z, vertical impulse; *W*, weight; *T*, wingbeat period; *U*, flight speed; *c*, wing chord.

the circulation of the strongest vortex. For this measure, the value taken at midwing is used, which can include oblique sections through continuous trailing vortices having smaller circulations at the centreplane because they do not usually extend over the midline. As represented by the dash-dot line, a weighted average of the two different Γ measures is used to model the most likely value.

The final result is shown in Fig. 33E, where the fraction of weight support provided by the E–R model wake vertical impulse is shown. The model results based on experimental Γ lie close to 1. The worst case is at the highest flight speed, and here the shortfall is likely to be the difficulty in correctly estimating the strength of vortices from streamwise cuts when the main structure is primarily streamwise also, and not spanwise. All data points lie within reasonable limits of I_z/WT=1. It is concluded that the wake model geometry and circulation estimates are self-consistent, and that this framework could be used to model bird wakes.

The only difficult input here was in knowing how to choose Γ, which was determined from experimental data in Fig. 33D. It would be useful to have a more general function, and so two empirical forms are given. The first approximates Γ with an arbitrary second order polynomial as:

$$\Gamma/Uc = C_0 + C_1U + C_2U^2 . \quad (31)$$

The vector of best-fit polynomial coefficients is C=[6.1, –1.08, 0.05] for the thrush nightingale wake. Alternatively, since one expects L and Γ to be related through Equation 11 ($L'=\rho U\Gamma$), then one might also predict that

$$\Gamma/Uc \approx C_1U^{-2} . \quad (32)$$

A reasonable fit to the data can be found by fixing the exponent to –2, when $C_1 \cong 40$.

The results of the E–R model have been expressed mostly in dimensionless form with a view to scaling them out to other cases than the single species examined here. At the same time, we also will refrain from further complicating a model whose basis still rests on the one (albeit extensive) dataset. Nevertheless, it is hoped that the current data, E–R model and limited generalisations from them will form the basis for a general model approach that can be successfully applied towards understanding and analysis of other aerodynamical problems in bird flight.

List of symbols

A_G	amplitude of Gaussian function (G)
A	wake segment area

AR	aspect ratio
b	wing semispan
c	mean chord
C_u	empirical coefficient for relative importance of upstroke wake
d, u	appearing as subscripts, denote downstroke and upstroke quantities
D	drag
f	wingbeat frequency
F_D	drag from wake momentum defect
$F_{x,z}$	net horizontal and vertical force (thrust and lift)
$\boldsymbol{g}$	gravity
G	Gaussian function
h	vertical wake height
$I_{x,z}$	horizontal, vertical wake impulse
k	reduced frequency
L	lift
L'	modified lift due to boundaries, lift per unit span
m	mass
Q	wing loading
r	radial coordinate
r_0	vortex core radius
R	span ratio
Re	Reynolds number
$\boldsymbol{S}$	material surface
S	wing area
S_e	projected area of wake ellipse
S'	equivalent cross-sectional area
t	time
t_c	characteristic evolution time (of wake segment)
T	wingbeat period
T_G	threshold of G
$\mathbf{u}$	velocity vector
u, v, w	components of $\mathbf{u}$ in x,y,z
u'	wake defect velocity
u_{rel}	relative velocity magnitude
U	flight speed
w_1	vertical induced velocity in late wake
W_z	mean vertical velocity
W	body weight
x,y,z	streamwise, spanwise and vertical directions
α	angle of incidence
δ	small increment, spatial resolution
Γ	circulation
Γ_{tot}	total circulation in and out of vortex cores
$\Gamma^{+,-}$	normalised circulation
Γ_0	reference circulation for weight support in steady, non-flapping flight
Γ_1	reference circulation for weight support by downstroke-shed ellipse
λ	wake wavelength
ν	kinematic viscosity
ρ	air density
ψ	wake segment inclination angle, measured from horizontal
σ	half-width of Gaussian function, G
τ	downstroke ratio
ω	vorticity vector
ω_y	component of vorticity in y (spanwise)
$\lvert\omega_y\rvert_{max}$	peak spanwise vorticity magnitude
$\Omega^{+,-}$	normalised vorticity

We are very grateful for the strong and continuous support of both Professors C. J. Pennycuick and T. Alerstam throughout this project. The research program was supported by the Knut and Alice Wallenberg foundation, the Carl Tryggers foundation and the Swedish Research Council (to A.H.). The experiments were carried out under licence from the Lund/Malmö Ethical Committee.

References

Alexander, R. McN. (1982). *Locomotion of Animals.* Glasgow: Blackie.

Alexander, D. E. (2002). *Nature's Flyers: Birds, Insects and the Biomechanics of Flight.* Baltimore: Johns Hopkins University Press.

Batchelor, G. K. (1967). *An Introduction to Fluid Dynamics*. Cambridge: Cambridge University Press.

Boratav, O. N., Pelz, R. B. and Zabusky, N. J. (1992). Reconnection in orthogonally interacting vortex tubes: direct numerical simulations and quantifications. *Phys. Fluids A* **4**, 581-605.

Cantwell, B. J. and Coles, D. (1983). An experimental study of entrainment and transport in the turbulent near wake of a circular cylinder. *J. Fluid Mech.* **136**, 321-374.

Dickinson, M. H., Lehmann, F.-O. and Sane, S. P. (1999). Wing rotation and the aerodynamic basis of insect flight. *Science* **284**, 1954-1960.

Farge, M. (1987). Normalization of high-resolution raster display applied to turbulent fields. In *Advances in Turbulence I* (ed. G. Comte-Bellot), pp. 111-123. Berlin: Springer-Verlag.

Farge, M. (1990). L'imagerie scientifique: choix des palettes de couleurs pour la visualisation des champs scalaires bidimensionnels. *L'Aeronautique et l'Astronautique* **140**, 24-33.

Fincham, A. M. and Spedding, G. R. (1997). Low-cost, high resolution DPIV for measurement of turbulent fluid flow. *Exp. Fluids* **23**, 449-462.

Hall, K. C. and Hall, S. R. (1996). Minimum induced power requirements for flapping flight. *J. Fluid Mech.* **323**, 285-315.

Hall, K. C., Pigott, S. A. and Hall, S. R. (1998). Power requirements for large-amplitude flapping flight. *J. Aircraft* **35**, 352-361.

Hedrick, T. L., Tobalske, B. W. and Biewener, A. A. (2002). Estimates of circulation and gait change based on a three-dimensional kinematic analysis of flight in cockatiels (*Nymphicus hollandicus*) and ringed turtle-doves (*Streptopelia risoria*). *J. Exp. Biol.* **205**, 1389-1409.

Hildebrand, M. (1965). Symmetrical gaits of horses. *Science* **150**, 701-708.

Katz, J. and Plotkin, A. (2001). *Low-Speed Aerodynamics.* 2nd edition Cambridge: Cambridge University Press.

Kokshaysky, N. V. (1979). Tracing the wake of a flying bird. *Nature* **279**, 146-148.

Lighthill, M. J. (1986). *An Informal Introduction to Theoretical Fluid Mechanics*. Oxford: Clarendon Press.

Norberg, U. M. (1990). *Vertebrate Flight.* Berlin: Springer-Verlag.

Pennycuick, C. J. (1968a). Power requirements for horizontal flight in the pigeon *Columba livia*. *J. Exp. Biol.* **49**, 527-555.

Pennycuick, C. J. (1968b). A wind tunnel study of gliding flight in the pigeon *Columba livia*. *J. Exp. Biol.* **49**, 509-526.

Pennycuick, C. J. (1975). Mechanics of Flight. In *Avian Biology*, vol. 5 (ed. D. S. Farmer, J. R. King and K. C. Parkes), pp. 1-75. London: Academic Press.

Pennycuick, C. J. (1988). On the reconstruction of pterosaurs and their manner of flight, with notes on vortex wakes. *Biol. Rev.* **63**, 299-331.

Pennycuick, C. J. (1989). *Bird Flight Performance: A Practical Calculation Manual*. Oxford: Oxford University Press.

Pennycuick, C. J., Alerstam, T. and Hedenström, A. (1997). A new low-turbulence wind tunnel for bird flight experiments at Lund University, Sweden. *J. Exp. Biol.* **200**, 1441-1449.

Pennycuick, C. J., Hedenström, A. and Rosén, M. (2000). Horizontal flight of a swallow (*Hirundo rustica*) observed in a wind tunnel, with a new

method for directly measuring mechanical power. *J. Exp. Biol.* **203**, 1755-1765.

Pennycuick, C. J., Heine, C. E., Kirkpatrick, S. J. and Fuller, M. R. (1992). The profile drag of a hawk's wing, measured by wake sampling in a wind tunnel. *J. Exp. Biol.* **165**, 1-19.

Pennycuick, C. J., Klaasen, M., Kvist, A. and Lindström, A. (1996). Wing beat frequency and the body drag anomaly: wind tunnel observations on a thrush nightingale (*Luscinia luscinia*) and a teal (*Anas crecca*). *J. Exp. Biol.* **199**, 2757-2765.

Prandtl, L. and Tietjens, O. G. (1934). *Applied Hydro- and Aeromechanics.* New York: Dover.

Rayner, J. M. V. (1979a). A vortex theory of animal flight. I. The vortex wake of a hovering animal. *J. Fluid Mech.* **91**, 697-730.

Rayner, J. M. V. (1979b). A vortex theory of animal flight. II. The forward flight of birds. *J. Fluid Mech.* **91**, 731-763.

Rayner, J. M. V. (1979c). A new approach to animal flight mechanics. *J. Exp. Biol.* **80**, 17-54.

Rayner, J. M. V. (1986). Vertebrate flapping flight mechanics and aerodynamics, and the evolution of flight in bats. In *Biona Report*, vol. 5 (ed. W. Nachtigall), pp. 27-74. Stuttgart: Gustav Fischer Verlag.

Rayner, J. M. V. (1991a). Wake structure and force generation in avian flapping flight. In *Bird Flight. Proc. 20th Int. Orn. Cong., Symp.* **9**, 702-715.

Rayner, J. M. V. (1991b). On aerodynamics and the energetics of vertebrate flapping flight. *Contemp. Math.* **141**, 351-400.

Rayner, J. M. V. (2001). Mathematical modeling of the avian flight power curve. *Math. Meth. Appl. Sci.* **24**, 1485-1514.

Rayner, J. M. V., Jones, G. and Thomas, A. (1986). Vortex flow visualizations reveal change in upstroke function with flight speed in bats. *Nature* **321,** 162-164.

Rayner, J. M. V. and Gordon, R. (1998). Visualization and modelling of the wakes of flying birds. In *Biona Report*, No. 13, *Motion Systems* (ed. R. Blickhan, A. Wisser and W. Nachtigall), pp. 165-173. Jena: Gustav Fischer Verlag.

Saffman, P. G. (1992). *Vortex Dynamics*. Cambridge: Cambridge University Press.

Spedding, G. R. (1981). The vortex wake of flying birds: an experimental investigation. PhD thesis, University of Bristol.

Spedding, G. R. (1986). The wake of a jackdaw (*Corvus monedula*) in slow flight. *J. Exp. Biol.* **125**, 287-307.

Spedding, G. R. (1987a). The wake of a kestrel (*Falco tinnunculus*) in gliding flight. *J. Exp. Biol.* **127**, 45-57.

Spedding, G. R. (1987b). The wake of a kestrel (*Falco tinnunculus*) in flapping flight. *J. Exp. Biol.* **127**, 59-78.

Spedding, G. R. (1992). The aerodynamics of flight. In *Adv. Comp. Physiol. The Mechanics of Animal Locomotion* (ed. R. McN. Alexander), pp. 51-111. Berlin: Springer.

Spedding, G. R. (2003). Comparing fluid mechanics models with experiment. *Phil. Trans. R. Soc. Lond. B* (in press).

Spedding, G. R., Rayner, J. M. V. and Pennycuick, C. J. (1984). Momentum and energy in the wake of a pigeon (*Columba livia*) in slow flight. *J. Exp. Biol.* **111**, 81-102.

Spedding, G. R. and Rignot, E. J. M. (1993). Performance analysis and application of grid interpolation techniques for fluid flows. *Exp. Fluids* **15**, 417-430.

Spedding, G. R. and DeLaurier, J. D. (1996) Animal and ornithopter flight. In *Handbook of Fluid Mechanics and Fluid Machinery*, Vol. 3: *Applications of Fluid Dynamics* (ed. J. A. Schetz and A. E. Fuhs), pp. 1951-1967. New York, John Wiley and Sons.

Spedding, G. R., Rosén, M. and Hedenström, A. (2003). Quantitative studies of the wakes of freely-flying birds in a low-turbulence wind tunnel. *Exp. Fluids* **34**, 291-303.

Tobalske, B. W. (2000). Biomechanics and physiology of gait selection in flying birds. *Physiol. Biochem. Zool.* **73**, 736-750.

Tobalske, B. W. and Dial, K. P. (1996). Flight kinematics of black-billed magpies and pigeons over a wide range of speeds. *J. Exp. Biol.* **199**, 263-280.

Tucker, V. A. (1990a). Body drag, feather drag and interference drag of the mounting strut in a peregrine falcon, *Falco peregrinus. J. Exp. Biol.* **149**, 449-468.

Tucker, V. A. (1990b). Measuring aerodynamic interference drag between a bird body and the mounting strut of a drag balance. *J. Exp. Biol.* **154**, 439-461.

White, F. M. (2003) *Fluid Mechanics* (5th edition). New York: McGraw-Hill.

Yan, J., Avadhanula, S. A., Birch, J., Dickinson, M. H., Sitti, M., Su T. and Fearing, R. S. (2002). Wing transmission for a micromechanical flying insect. *J. Micromechatronics* **1**, 221-237.

Zabusky, N. J., Fernandez, V. M. and Silver, D. (1995). Collapse, intensification and reconnection in vortex dominated flows: visiometrics and modeling. *Physica D* **86**, 1-11.